JGR Solid Earth

RESEARCH ARTICLE
10.1029/2021JB023246

Crustal Structure Beneath the Northern Appalachians and the Eastern Grenville Province

Omid Bagherpur Mojaver[1] **and Fiona Darbyshire**[1]

[1]Centre de Recherche Geotop, Université du Québec à Montréal, Montreal, QC, Canada

Key Points:

- Crustal thickness and velocities in eastern Canada are more variable in the Peri-Gondwanan than Peri-Laurentian domains
- A step-like Moho feature in the northern Appalachians marks the boundary between the Peri-Gondwanan and Peri-Laurentian domains at depth
- The lower crust in the Grenville Province is thicker and faster than that observed beneath the northern Appalachians

Supporting Information:

Supporting Information may be found in the online version of this article.

Correspondence to:

O. Bagherpur Mojaver,
omid.bagherpur@gmail.com

Citation:

Bagherpur Mojaver, O., & Darbyshire, F. (2022). Crustal structure beneath the northern Appalachians and the eastern Grenville Province. *Journal of Geophysical Research: Solid Earth*, *127*, e2021JB023246. https://doi.org/10.1029/2021JB023246

Received 14 SEP 2021
Accepted 28 DEC 2021

Abstract Southeastern Canada and the northeastern USA include terranes that were tectonized since the Archean, making this region an excellent place to investigate the evolution of continental crust. Our study area covers the Archean southeastern Superior Province, the Proterozoic eastern Grenville, and the Phanerozoic northern Appalachians comprising terranes with either Peri-Laurentian or Peri-Gondwanan heritage. Adopting a Rayleigh wave ambient noise tomography method, we used noise data recorded between 2013 and 2015, and obtained high resolution anisotropic tomographic images of the crust enabling us to discuss tectonic implications. The azimuthal anisotropy orientations follow a dominant NE-SW trend across the study area, but some localized changes of anisotropy direction in the Bay of Fundy and across the Appalachian front are observed. The crust beneath the older Superior and Grenville provinces is generally fast, whereas the Appalachians include strong slow anomalies, especially at upper crustal depths, where they represent thick sedimentary basins beneath the St. Lawrence valley, the Gulf of St. Lawrence, and the Bay of Fundy. We suggest that the boundary between the Peri-Laurentian and the Peri-Gondwanan terranes at depth is marked by a Moho-offset feature observable in our models. A generally similar crustal seismic signature for the two youngest easternmost tectonic domains suggest that they were never separated by a wide ocean basin. Our results provide important evidence for evolution of the continental crust during and after accretionary/collisional episodes in the study area.

Plain Language Summary Southeastern Canada and the northeastern USA comprise rocks that preserve the formation and evolution of continental crust over at least 2.5 billion years, making this region an ideal place to improve our understanding of the processes that created today's continents, such as rifting or mountain building. Seismic noise data recorded by a network of stations can be analyzed to model crustal structure, using the speed at which seismic waves travel through the crust at different depths, and the resulting models help us to understand how the crust was formed and modified over geological time. We used more than 2 yr of seismic noise datasets and measured the variations of seismic velocity structure in different crustal layers, as well as the total thickness of the crust across the study area. We observed that the younger crustal domains have a more complex upper layer structure than the older units. The older domains, however, have a faster and thicker lower crustal layer than the younger zones. Beneath the central younger domains of the northern Appalachians, we observed that the crustal thickness varies over a short distance, creating a step-like geometry for the base of the crust.

1. Introduction

Eastern North America is an important place to investigate the implication of the theory of plate tectonics. This is due to geological units in this area preserving a protracted history of formation and evolution for ages varying from Archean to Phanerozoic. Discussing tectonic implications for such a complex region requires a deep understanding of the crustal structure. To this end, seismic tomography models are extremely valuable as they can provide us with a detailed look at the velocity structure at different scales. With the aim of obtaining high resolution tomographic images of the crust and sub-Moho structure beneath southeastern Canada and the NE United States, we used recent records of broadband seismic data in a passive seismic technique, namely Ambient Noise Tomography (ANT; Shapiro & Campillo, 2004; Shapiro et al., 2005), that has been successful in recovering detailed crustal and uppermost mantle velocity structure in regional-scale (e.g., Green et al., 2017; Kuponiyi et al., 2017; Lin et al., 2008; McLellan et al., 2018; Pawlak et al., 2012; Y. Yang et al., 2008) and continental scale (e.g., Bensen et al., 2008; Kao et al., 2013; Y. Yang et al., 2007) studies. Recently added data coverage in our study area, in the years from 2013 to 2015, provides us with an unprecedented opportunity to recover the highest

resolution anisotropic velocity structure of the crust and sub-Moho depths to date. We use our models along with previous geophysical constraints to discuss tectonic implications.

1.1. Tectonic Setting

Our study area spans ~3/4 of Earth's geological history with geological units that were formed and tectonized from Archean to Mesozoic. The three major tectonic provinces from the oldest to youngest are the Archean southeastern Superior Province, the Proterozoic eastern Grenville, and the Phanerozoic northern Appalachians.

In the far northwest of the study area, a small part of the southeastern Superior Province including the eastern Abitibi subprovince and the northeastern Pontiac domain are covered by this study. These tectonic domains comprise a collage of mafic to felsic volcanic units with ages ranging from 2,750 to 2,690 Ma (e.g., Ludden & Hynes, 2000). The Grenville front marks the NW limit of the Grenvillian metamorphism and deformation, and separates the Superior from the eastern Grenville Province (e.g., Rivers et al., 1989). The Grenville Province arises from a ~300 Ma period of accretions and orogenesis coinciding with the final assembly of the supercontinent Rodinia at ~1 Ga (Whitmeyer & Karlstrom, 2007). Based on deformation, metamorphism, and geophysical contraints, the eastern Grenville orogen is divided into three first order belts including Parautochthonous Belt (PB), Allochthonous Monocyclic Belt (AMB), and Allochthonous Polycyclic Belt (APB; e.g., Rivers, 2008). In the northwest of the Grenville, sub-parallel to the Grenville front, the PB is associated with high pressure and temperature Grenvillian metamorphism representing a section of exhumed Laurentian crust overlying a southeast dipping parautochthonous Archean basement (e.g., Rivers, 2015). The AMB consists of exotic terranes accreted to Laurentia between 1,080 and 1,035 Ma (Carr et al., 2000). The APB covers the majority of the Grenville Province and comprises terranes originally part of a Laurentian continental margin arc setting and preserves evidence of Paleoproterozoic to early Mesoproterozoic metamorphism overprinted by metamorphism of Grenvillian age (Rivers et al., 2002). The Grenvillian orogeny occurred in two phases, namely Ottawan and Rigolet phases (Darbyshire et al., 2017; Rivers, 2015). The Ottawan orogenic phase (~1,090 to 1,020 Ma) is restricted to the Allochthonous terranes and characterized by a high grade metamorphic signature, and a period of significant crustal shortening and thickening resulting in formation of an orogenic plateau. The relatively long-duration Ottawan phase was followed by the much shorter (~1,005 to 980 Ma) Rigolet phase that was restricted to the Parautochthonous terranes along the hanging wall of the Grenville front.

The Appalachian front is a first order structural boundary separating the Grenville Province from the northern Appalachians. The northern Appalachians were tectonized during four orogenic episodes occurring from 485 to 350 Ma (van Staal et al., 2009, 2012). Accretion of terranes during these orogenic episodes coincided with rift-drift processes associated with the opening and closing of the Iapetus and Rheic Oceans (Hibbard, van Staal, & Miller, 2007). Tectonic domains in the northern Appalachians from west to east (i.e., oldest to youngest) are the Humber margin, Dunnage zone, Ganderia, Avalonia, and Meguma. Terranes belonging to these domains have either Gondwanan or Laurentian provenance. Accretion of the terranes currently situated in the Humber margin and the Dunnage zone occurred during the Taconic orogeny (485–450 Ma; van Staal & Barr, 2012). The Humber margin extends along the eastern edge of the Appalachian front and records opening of a Taconic seaway and the Iapetus Ocean at 615 Ma (Hibbard, van Staal, & Rankin, 2007; Kamo et al., 1989). The Dunnage zone comprises intra-oceanic terranes originally belonging to Gondwana or Laurentia with a faulting system, named Red Indian Line, separating the Gondwanan and Laurentian units (Macdonald et al., 2014; Williams et al., 1988). The three coastal domains of the northern Appalachians, namely Ganderia, Avalonia, and Meguma, include Peri-Gondwanan realms that accreted to eastern Laurentia during three different orogenic episodes: the Salinic (450–423 Ma), Acadian (421–400 Ma), and Neo-Acadian (395–350 Ma; Levin et al., 2017; van Staal et al., 2009, 2012). Ganderia was rifted from Gondwana in the late Neoproterozoic and accreted to eastern North America in the late Ordovician to early Silurian, closing the Iapetus Ocean (van Staal et al., 2012; Wilson et al., 2017). Avalonia was accreted to the Ganderia passive margin during the late Silurian to early Devonian Acadian orogeny. Lastly, accretion of Meguma to eastern North America occurred during the middle Devonian to early Carboniferous Neo-Acadian orogeny. The northern Appalachian orogenesis was terminated by collision of Gondwana and composite Laurentia in the Carboniferous-Permian Alleghanian orogeny resulting in the formation of supercontinent Pangea (van Staal & Barr, 2012). Accretion-related structures in the present-day northern Appalachians have escaped from Alleghanian modifications as the suture zone was far, and is now concealed in

the margins of the Atlantic Ocean (van Staal & Barr, 2012). Accordingly, pre-Alleghanian tectonic history in the northern Appalachians is mostly well preserved.

The Canadian Appalachians have been tectonically quiet since the Cretaceous, and the latest tectonic activity was during the breakup of Pangea resulting in development of the Eastern North American rift systems that include the Fundy basin (Withjack et al., 2009). The formation of the Bay of Fundy was due to orogen-perpendicular (NW-SE) rifting that started in the Middle Triassic, which also activated NE trending compressional structures as normal faults (Withjack et al., 1995). Rifting ceased in the Bay of Fundy when Early to Middle Jurassic continental breakup led to the opening of the North Atlantic Ocean (Funck et al., 2004; Withjack et al., 2009).

1.2. Previous Seismic Studies

Thanks to the Lithoprobe project in the 1990s (e.g., Clowes, 2010) and installation of temporary broadband seismographs in the last ~20 yr (e.g., Eaton et al., 2005), seismology has significantly improved our understanding of the structure of eastern Canada at crustal and uppermost mantle depths. Seismic structure in different parts of our study area has been investigated at different scales and depth ranges using various techniques including ANT (e.g., Bensen et al., 2009; Kao et al., 2013; Kuponiyi et al., 2017), earthquake-based tomography (e.g., Bagherpur Mojaver et al., 2021; Boyce et al., 2016; Petrescu et al., 2017; Schaeffer & Lebedev, 2014; Shen & Ritzwoller, 2016), joint inversion of seismic ambient noise and earthquake data (Golos et al., 2018), receiver function methods (e.g., Levin et al., 2017; Li et al., 2018, 2020; Petrescu et al., 2016), shear wave splitting measurements (e.g., Darbyshire et al., 2015; Gilligan et al., 2016; Long et al., 2016; B. B. Yang et al., 2017), and reflection-refraction seismic profiling (e.g., Clowes, 2010; Cook et al., 2010; Hammer et al., 2010; Ludden & Hynes, 2000). In this section we provide a brief review of the previous findings.

Using ambient seismic noise data, a few continental-scale studies modeled the seismic structure of the crust and uppermost mantle in our study area (e.g., Bensen et al., 2009; Kao et al., 2013). According to their models, seismic structure of the crust beneath the northern Appalachians appears to be more complex than the Precambrian domains. An interesting observation is a large velocity gradient recovered throughout different parts of the Canadian Shield at mid-crustal depths and up to about the Appalachian front, interpreted as a relict rheological boundary between the upper and lower crust (Kao et al., 2013). The Gulf of St. Lawrence at depths <20 km is dominated by slow anomalies (Kao et al., 2013). A regional-scale study carried out over this area suggests a maximum sedimentary thickness of ~8 km beneath this region (Kuponiyi et al., 2017). It is also suggested that the Grenvillian basement beneath the northern Appalachians is wedged out at depth by the Red Indian Line (Kuponiyi et al., 2017). Adopting a probabilistic joint-inversion scheme, Shen and Ritzwoller (2016) used receiver functions, group, and phase velocities from ambient noise and earthquakes, and Rayleigh wave ellipticity measurements, and obtained high resolution shear velocity models at crustal and uppermost mantle depths across the entire USA. A noteworthy observation of their final crustal thickness map is a ~8 km Moho depth contrast with NE-SW trend over a relatively small distance within the northern Appalachians.

Variations in crustal thickness and bulk crustal composition beneath our study area have been investigated through seismic methods of receiver functions (Levin et al., 2017; Petrescu et al., 2016), reflection-refraction seismic profiling (e.g., Cook et al., 2010), and surface wave tomography (e.g., Bagherpur Mojaver et al., 2021; Kao et al., 2013). Results from the reflection-refraction seismic profiles suggest that the Moho depths beneath our study area vary from ~30 to 45 km (Hall et al., 1998; Ludden & Hynes, 2000). Available receiver function studies carried out over our study area suggest that the crustal thickness varies between ~25 and ~50 km, with more small-scale variations of crustal thickness and V_p/V_s ratio occurring beneath the Appalachians than the older Precambrian domains (Levin et al., 2017; Petrescu et al., 2016). These results also indicate that the greatest complexity of crustal properties (crustal thickness, Moho thickness, and V_p/V_s ratio) occurs across the Appalachian front (Levin et al., 2017). Crustal and lithospheric thickness estimates from a previous surface wave study and active seismic profiles do not suggest a simple relation for the thickness of these layers with the age of the terranes, and a generally thinner crust and lithosphere is suggested beneath the central part of the Appalachians (Bagherpur Mojaver et al., 2021; Hall et al., 1998). Using receiver functions with broadband datasets spanning more than 20 yr, a detailed look at the crustal structure of the Grenville and Appalachian provinces beneath the northeastern USA is presented by Li et al. (2018, 2020). They note crustal thickness variations roughly correlated with surface elevation and anticorrelated with Bouger gravity anomaly, sharp Moho steps with maximum offset

of 15 km within narrow zones, and an eastward decrease of Moho thickness. These results are indicative of a very complex 3D crustal structure beneath our study region.

Among the reflection-refraction seismic profiles carried out during the Lithoprobe project, several profiles belonging to the Abitibi-Grenville transect (AG; lines 52, 53, and 54 in the Grenville Province; Ludden & Hynes, 2000), and the Lithoprobe-East transect (LE; lines 86/1, 86/2, 86/4, 86/5, and 88/1 in Gulf of St. Lawrence; Hall et al., 1998) lie within our study area. Although results from other profiles outside the study area are still useful (e.g., Newfoundland), we note that caution must be exercised in translating their conclusions into our study area. This is mainly because the Laurentian margin had a very irregular shape before the Paleozoic accretionary events (Stockmal et al., 1987). The study of active seismic profiles in the Appalachians suggests that the Grenvillian basement is at least extended beneath the Humber margin and part of the Dunnage zone, and it is distinguished by strong mid-crustal reflectors, moderately strong lower crustal reflectors, and relatively deep Moho depths (Hall et al., 1998). It is also suggested that the Superior craton continues as a wedge into the Grenville lower crust 200–300 km southeast of the Grenville front (Ludden & Hynes, 2000; Rivers, 1997). Interpretation of the Lithoprobe AG lines in the Grenville suggests that the southeast dipping reworked Archean basement is less extended beneath our study area compared to the farther southwest Lithoprobe profiles in the Grenville Province (Ludden & Hynes, 2000). It is suggested that the mafic intrusive unit in the eastern portion of the AMB domain is underlain by high pressure terranes at least down to the Moho discontinuity, whereas in the western AMB, where a different allochthon unit is observed at the surface, underlying crustal structures are interpreted as two layers of high pressure terranes underlain by another layer of SE dipping Laurentian Archean material that was reworked during the Rigolet phase (Ludden & Hynes, 2000). Interesting findings of the active seismic profiles in the Appalachians include a generally thinner crust beneath the central part of the orogen relative to the continental margin and the western domains, and high velocity lower crust beneath the profiles over the Gulf of St. Lawrence which requires a mafic composition (Hall et al., 1998).

Global (e.g., Ritsema & Lekić, 2020; Schaeffer & Lebedev, 2013) and continental-scale (e.g., Clouzet et al., 2018; Schaeffer & Lebedev, 2014; Shen & Ritzwoller, 2016) tomographic models suggest an overall faster Superior and Grenville Province relative to the Appalachians. Available regional-scale tomographic studies observe clear systematic differences of seismic signatures for the three major tectonic domains with typically decreasing lithospheric mantle velocities from the Archean Superior to the Phanerozoic Appalachians (e.g., Boyce et al., 2016). A regional-scale study suggests a two-stage lithospheric formation beneath the North American Craton (Petrescu et al., 2017). In the northern Appalachians, systematic differences are observed between the lithospheric seismic velocities of the Peri-Laurentian terranes (i.e., Humber margin and parts of the Dunnage zone) and the Peri-Gondwanan terranes (i.e., parts of the Dunnage, Ganderia, Avalonia, and Meguma domains; Bagherpur Mojaver et al., 2021; Yuan et al., 2014). A NW-SE trend of slow anomalies crosscutting the three major tectonic domains in eastern Canada is interpreted as resulting from the passage of the Great Meteor Hotspot (GMH) during Mesozoic times (Boyce et al., 2016; Villemaire et al., 2012). Spatially coincident with the passage of the GMH, a strong slow anomaly in the northern Appalachians (Northern Appalachian Anomaly; NAA) is observed at depths from 60 to 100 km (e.g., Bagherpur Mojaver et al., 2021; Golos et al., 2018). It is interpreted as resulting from either compositional changes caused by the GMH tectonism (e.g., Boyce et al., 2016; Villemaire et al., 2012), or due to a small-scale convection process (Menke et al., 2016).

Several studies have modeled seismic anisotropy beneath the broadband seismographs of the study area using shear wave splitting techniques (e.g., Darbyshire et al., 2015; Gilligan et al., 2016; B. B. Yang et al., 2017). Shear wave splitting measurements give integrated anisotropy information over a wide range of depths from the base of the mantle to the surface. The relatively large splitting times (>1 s) suggest contribution of both lithosphere and asthenosphere (Darbyshire et al., 2015; B. B. Yang et al., 2017). Multiple layers of anisotropy are suggested beneath southeastern Canada and the northeastern USA (Long et al., 2016). A generally parallel to subparallel trend of the splitting directions relative to the tectonic trend, weak correlation with the direction of absolute plate motion, and observed complex and small-scale variations of the anistropy orientation and magnitude suggest a more significant role for the lithosphere compared to asthenosphere in our study area (e.g., Darbyshire et al., 2015; Gilligan et al., 2016). Another study carried out over the NE USA, however, suggests that the observed anisotropy is mostly from the upper asthenosphere (B. B. Yang et al., 2017). The role of the crust in the observed anisotropy across our study area is not discussed in the available shear wave splitting measurements. In this case, constraining seismic anisotropy using surface wave tomography techniques can shed light on this issue, and has

the advantage of giving depth-dependent (period-dependent) information as opposed to the depth-averaged shear wave splitting measurements.

2. Data and Method

2.1. Data and Data Processing

The data used in this study are continuous vertical component seismograms belonging to 69 broadband stations from six different seismograph networks (Figure 1b). The seismic networks are the Canadian National Seismograph Network (CN; Geological Survey of Canada, 1989), New England Seismic Network (NE; Albuquerque Seismological Laboratory (ASL)/USGS, 1994), USArray Transportable Array (TA; IRIS Transportable Array, 2003), Portable Observatories for Lithospheric Analysis and Research Investigating Seismicity (PO: POLARIS; Eaton et al., 2005), and QM-III experiment (X8 and Y8 networks; Menke et al., 2012; SEIS-UK, 2013). The stations belonging to the TA and QM-III networks were only operational in 2013–2015, and combined with the data from other networks during that period, they provide us with the inter-station path coverage required to recover high-resolution seismic velocity models across the study area.

The data acquisition process was carried out for the available daily records of all stations from 1 August 2013 to 1 November 2015 (823 days). Some daily records were rejected due to instrument irregularities and data fragmentation issues, resulting in a variable number of daily records from 362 to 823 days, with an average of 716 days, for the stations. We followed the recommended procedure of Bensen et al. (2007) for data processing, except for the temporal normalization step where we chose to apply one-bit normalization instead of the running absolute mean normalization method (e.g., Shapiro & Campillo, 2004; Shapiro et al., 2005; Yao et al., 2006). Accordingly, single station data processing steps applied to the daily records include removing the data trend and mean, resampling of time-series to a common sampling rate of 1 Hz, instrument response removal, one-bit normalization to exclude the earthquake signals, and spectral whitening to flatten the ambient seismic noise in the frequency domain (Bensen et al., 2007).

By stacking long-duration noise cross-correlation time series, the Empirical Green's Functions (EGFs) will emerge (e.g., Shapiro & Campillo, 2004). The positive (causal) and negative (acausal) parts of the EGFs represent waves traveling in opposite directions between the station pairs, and the same physics as that used in surface wave analysis can be applied to these dispersive wavetrains to extract phase velocity information for the paths between the stations (e.g., Y. Yang et al., 2008). We calculated EGFs for all possible station pairs, resulting in more than 2,340 EGFs with the stack number varying from 81 to 823 days, and average stack number of 650 days. Since our study area is located next to the Atlantic coast, the energies of the emerging wavetrains for the causal and acausal signals are significantly different (Figure 2). This could cause bias in the measurement of phase velocities from the noise correlation functions (e.g., Tian & Ritzwoller, 2015). To quantify the bias due to non-uniform noise distribution in our measurements of phase velocities, we investigated different dataset scenarios generated from different time periods of stacking. By comparing the results from a selected semi-homogeneous dataset to the ones from our final inversions, we conclude that our final phase velocity measurements are reliable regardless of the observable non-uniform noise distribution in the data (see Supporting Information S1 for discussion).

2.2. Dispersion Measurements

We calculated the inter-station Rayleigh wave phase velocity dispersion curves from the inter-station EGFs using the *GSpecDisp* program (Sadeghisorkhani et al., 2018). This is a MATLAB-based GUI software that is primarily designed to facilitate phase velocity dispersion measurements from stacked noise correlation functions in the spectral domain. There are two main modules included in this program that are developed for calculating a regional average dispersion curve (method of Prieto et al., 2009), as well as individual inter-station dispersion curve measurements (method of Ekström et al., 2009). Although an automatic selection process is available in this program, we manually selected the phase velocity measurements for all the EGFs.

For measuring phase velocities from the input stacked correlation functions at each period, the real part of the input EGF spectrum is matched with the zero crossings of appropriate Bessel functions. Phase velocity is obtained using the formula

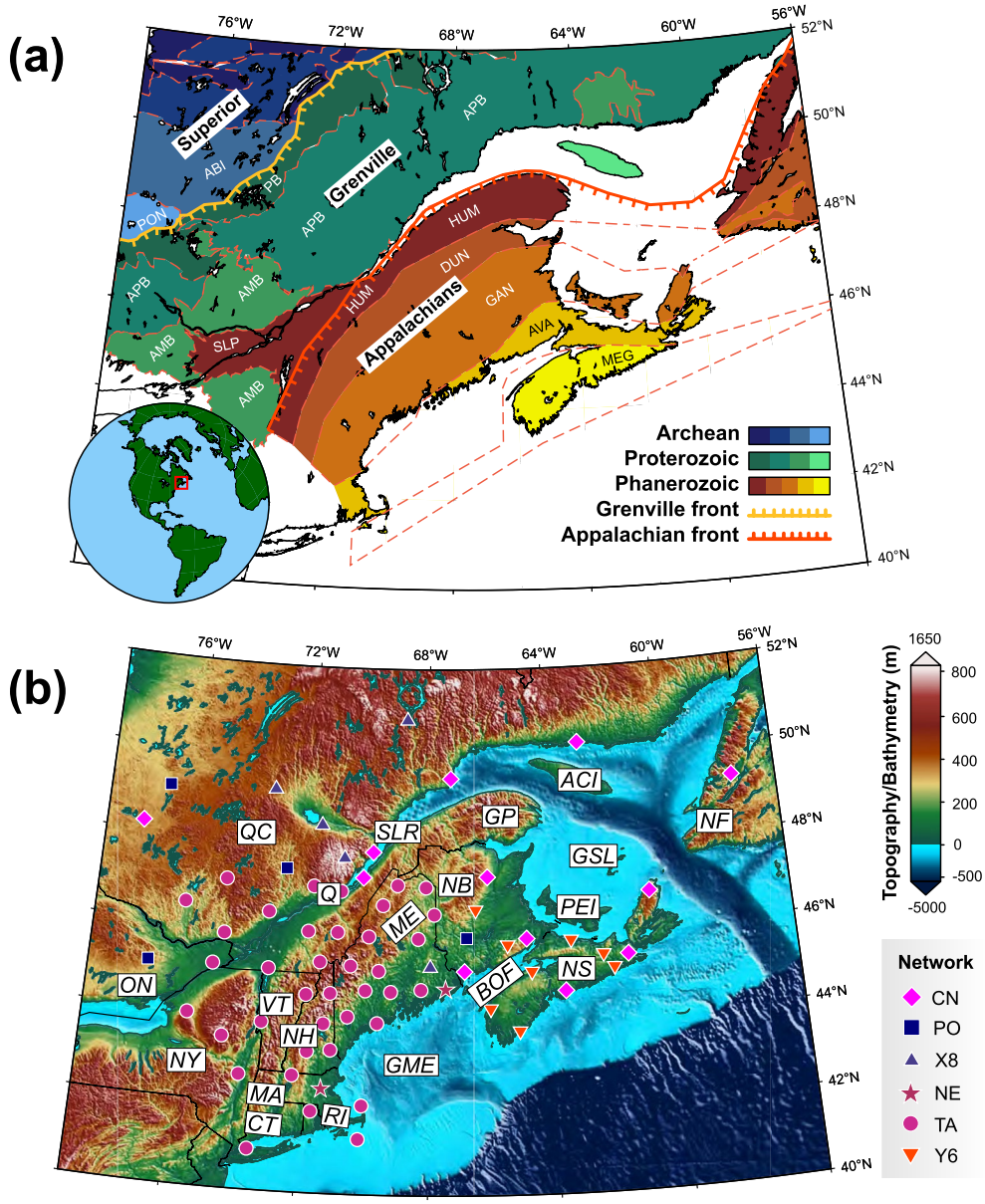

Figure 1. (a) Simplified tectonic map of eastern Canada. ABI: Abitibi subprovince, AMB: Allochthonous Monocyclic Belt, APB: Allochthonous Polycyclic Belt, AVA: Avalonia, DUN: Dunnage zone, GAN: Ganderia, HUM: Humber margin, MEG: Meguma, PB: Parautochthonous Belt, PON: Pontiac domain, SLP: St. Lawrence platform. (b) The 69 broadband seismic stations belonging to 6 seismograph networks overlain on topography/bathymetry of the study area. ACI: Anticosti Island, BOF: Bay of Fundy, CT: Connecticut, GME: Gulf of Maine, GP: Gaspé Peninsula, GSL: Gulf of St. Lawrence, MA: Massachusetts, ME: Maine, NB: New Brunswick, NF: Newfoundland, NH: New Hampshire, NS: Nova Scotia, NY: New York, ON: Ontario, PEI: Prince Edward Island, Q: Quebec City, QC: Quebec (Province), RI: Rhode Island, SLR: St. Lawrence River, VT: Vermont.

$$C(\omega_n) = \frac{\omega_n}{Z_n + 2m}$$

where Z_n denotes the n-th zero crossing of the Bessel function, ω_n is the angular frequency of the n-th zero-crossing of the correlation spectrum, and $m = 0, \pm1, \pm2, \ldots$ takes the 2π ambiguity of phase velocity (cycle skipping) into account. Due to the values of m, many possible dispersion curves can be measured for an EGF. Using the average dispersion curve measurement module of *GSpecDisp*, we first calculated a few different average dispersion curves by dividing the study area into sub-regions, based on geology and tectonics. Next, we used those average

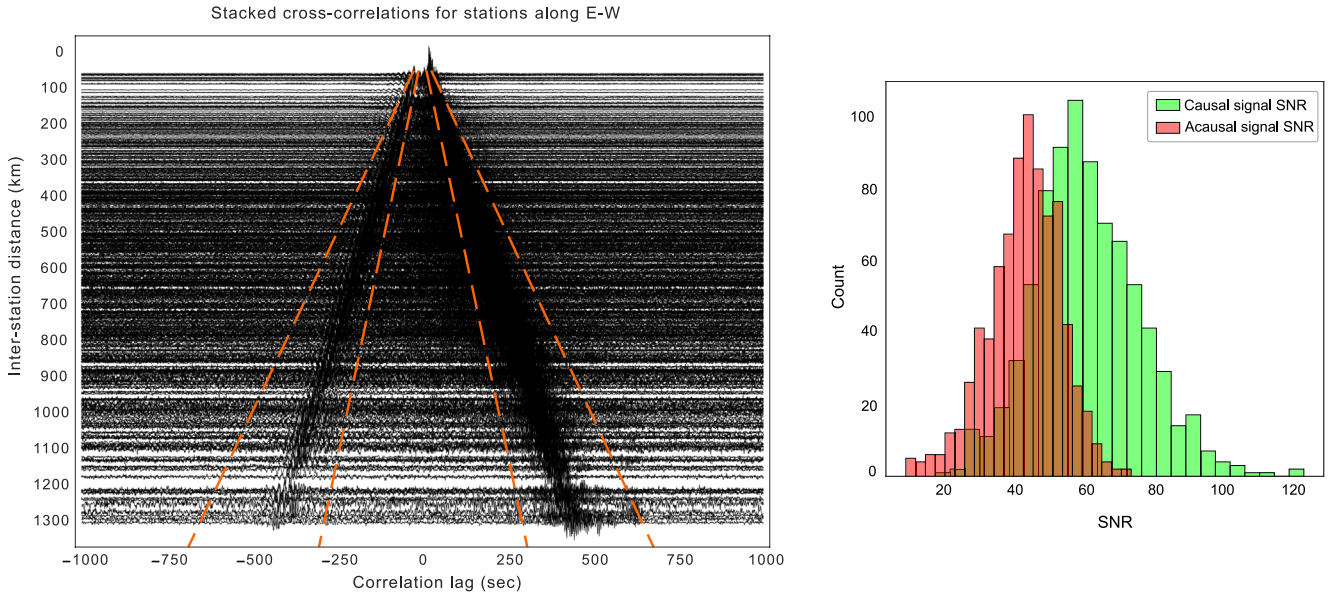

Figure 2. (Left) calculated EGFs for a subset of E-W paths between stations. Causal (positive lag) signals: east to west propagation, acausal (negative lag) signals: west to east propagation. The moveout lines (orange dashed lines) are drawn for 2 and 4.5 km/s velocities. (Right) distribution of signal-to-noise ratios for causal/acausal signals related to all EGFs from E-W paths measured in this study.

curves as references to manually select the appropriate phase velocities for individual inter-station paths. A few representative examples of the individual dispersion measurements, as well as the regional average dispersion curve for the study area, are illustrated in Figure 3. As shown in this figure, reliable phase velocity measurements at the longest periods (e.g., >40 s) can only be achieved from EGFs with longer inter-station distances (e.g., E55A-I64A and VLDQ-I64A in Figure 3).

2.3. Tomography Method

There are direct and indirect approaches to extract shear velocity models from surface waves. In the first approach, surface waves are directly inverted for a shear wave velocity model (e.g., Debayle & Kennett, 2000; van der Lee & Frederiksen, 2005). Alternatively, phase or group velocity maps at different periods are extracted as the first step of the tomography procedure and then inverted for shear velocity information (e.g., Kao et al., 2013; Kuponiyi et al., 2017). In this study, we first recover Rayleigh wave phase velocity variations at discrete periods from the calculated inter-station dispersion measurements, and then we extract 1D dispersion curves from the generated phase velocity maps to be inverted for shear velocity profiles.

The tomography program requires the input inter-station phase velocities to also include measurement errors. However, the *GSpecDisp* program does not give the measurement errors. In this case, a fixed set of synthetic errors (baseline errors) is assigned to the measurements, with errors typically increasing with increasing period and ranging from 0.015 to 0.040 km/s. We argue that the measurement errors should be proportional to the EGF quality such that smaller phase velocity errors should be attributed to higher quality EGFs. Therefore, we calculated the signal-to-noise ratios (SNR) for the symmetrized EGFs and used the mean of these values as a reference to modify the baseline errors for each inter-station dispersion curve (increase/decrease by a maximum of $\sim\pm$0.01 km/s from the baseline errors). Since the distribution of the calculated SNR values is very similar to a Gaussian distribution, we used the z-score (i.e., a real number that is the distance from the distribution mean given in terms of the number of standard deviations) of the SNR for each EGF and multiplied it by a small value of 0.002 to estimate the error adjustments from the baseline errors for each period of the inter-station dispersion curves. This small value was decided experimentally after making sure that it does not cause the final measurement errors to be negative or too strongly deviated from the reference errors. The assigned measurement errors for periods in this study, 4–50 s, before and after the error adjustment process are 0.015–0.04 km/s and 0.0092–0.0438 km/s, respectively.

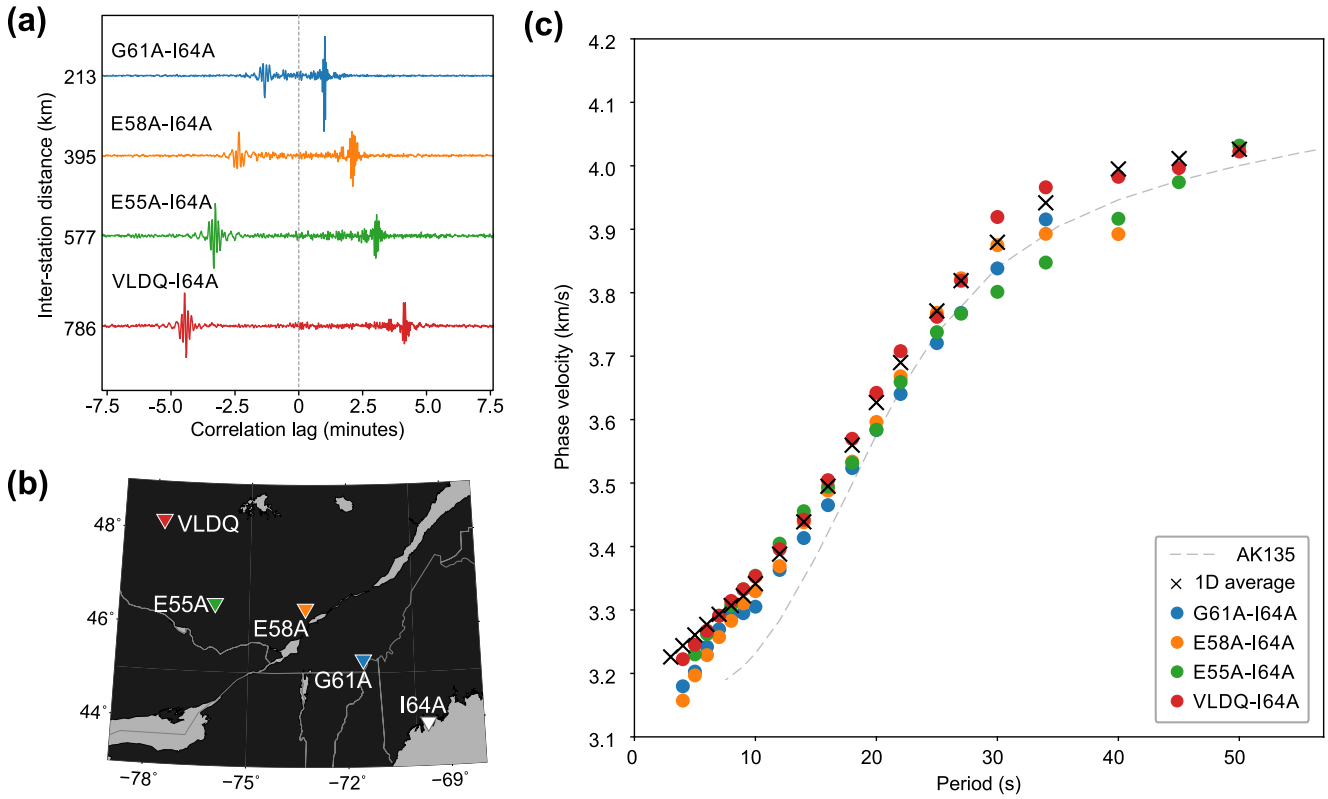

Figure 3. (a) Examples for EGFs related to station I64A cross-cutting various tectonic domains in the study area. (b) Map of the stations related to the shown EGFs. (c) Measured inter-station dispersion curves for the shown EGFs. The 1D average curve (cross symbols) represents the regional average based on all EGF measurements.

We followed the tomography method described by Darbyshire and Lebedev (2009) to recover anisotropic phase velocity variations at periods from 4 to 50 s. This inversion method has been successfully implemented in previous studies using earthquake-based 2-station phase velocities (e.g., Deschamps et al., 2008; Foster et al., 2020; Petrescu et al., 2017), earthquake-to-station group velocities (e.g., Darbyshire et al., 2018), ambient-noise group velocities (e.g., Pawlak et al., 2012), and combined ambient-noise and earthquake 2-station phase velocities (e.g., McLellan et al., 2018). The inversion is performed across a triangular grid of nodes that are evenly spaced throughout the region covered by the surface wave raypaths. We set the model and interpolation grid spacing to 80 and 20 km, respectively.

Assuming a weakly anisotropic medium, the inversion solves for five unknowns in phase velocity at each node:

$$\delta C(\omega) = \delta C_{iso}(\omega) + A_1\cos(2\psi) + B_1\sin(2\psi) + A_2\cos(4\psi) + B_2\sin(4\psi)$$

where δC_{iso} is the isotropic phase velocity anomaly, and 2ψ and 4ψ are the anisotropic components for the phase velocity variations with π and $\pi/2$ periodicity, respectively (Smith & Dahlen, 1973). The inversion algorithm is a least-squares technique with regularization terms (norm and roughness of the model) added to the cost function in addition to the data-model misfit term in its formulation. The solutions are found by solving a system of linear equations governing relations between the average phase velocity along the paths, the horizontal sensitivity area at the grid nodes (assuming zero-width rays), and phase velocity perturbations over the model grid. The model is regularized by adding smoothing and damping terms into the inversion kernel matrix that penalize the first and second derivatives of the recovered anomaly distribution. The damping applied by penalizing the second derivative of the variations for the neighboring nodes diminishes the patterns of anisotropy more strongly. Therefore, applying much larger smoothing parameters compared to the damping parameters is required (Figure 4; Foster et al., 2020). We tested many different regularization parameter values for isotropic and anisotropic components and chose an appropriate setting based on the regularization trade-off curves between the variance reduction and model roughness, as well as visual assessment of the resulting phase velocity maps. The isotropic and anisotropic regularization curves show the expected shape of trade-off curves, making it possible to select best approximate

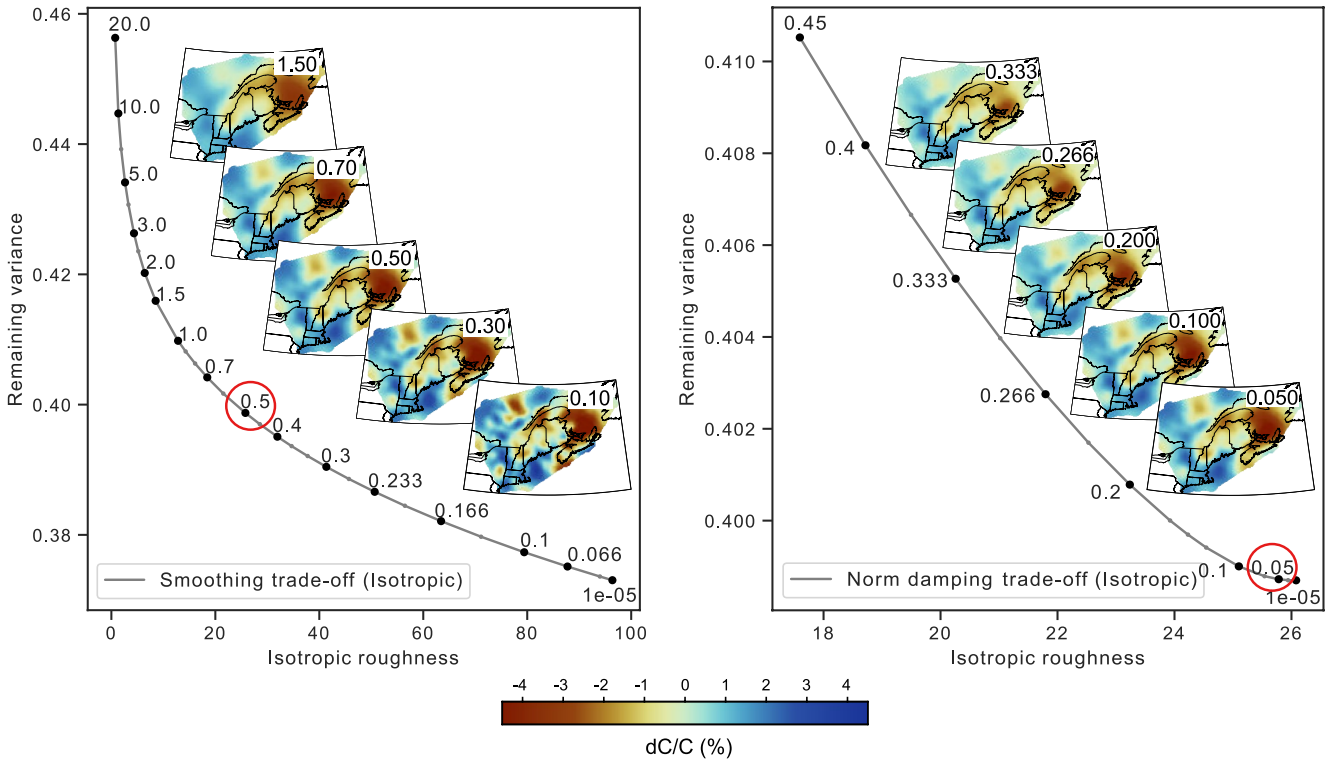

Figure 4. Inversion regularization trade-off curves for 16 s period. (Left) smoothing trade-off curve. (Right) damping trade-off curve. The red circles mark the values used in the final inversions. The maps illustrate the inversion results for the regularization parameter values marked at the top right corner of the maps. Only curves for the isotropic component are shown here (see Figures S5 and S6 in Supporting Information S1 for the other components).

values from the curve knees (Figure 4; Figures S5 and S6 in Supporting Information S1). Since the resolution of the anisotropic components is generally lower, they were more strongly damped and smoothed (e.g., Darbyshire & Lebedev, 2009). We investigated the regularization trade-off curves at multiple periods and found that regardless of the period, the optimal values of smoothing and damping stay constant. As a result, we applied the same regularization parameters in the inversions to the phase velocity datasets at all periods for consistency (Table S2 in Supporting Information S1).

Depending on the background noise level at the seismograph sites, the inter-station distance, and the number of stacked noise cross-correlation functions used in the generation of the EGFs, the frequency content of the dispersion measurements varies for different paths. This results in a notable difference in the path coverage at different periods. The number of crossing raypaths varies from a minimum of 183 (50 s period) to a maximum of 1,429 (6 s period) with an average of 1,106 rays (Figure S1 in Supporting Information S1).

The dispersion datasets that were input to the tomography program must satisfy the following two criteria:

1. The time domain SNR must be higher than 8.8 dB for the symmetrized EGFs (Figure S4 in Supporting Information S1). This value is calculated using the $\mu - 2\sigma$ formula for the SNR distribution of all possible EGFs, where μ is the mean SNR for the distribution, and σ is the standard deviation of the calculated SNR values. We use the formula $SNR(dB) = 20\log\left(\frac{RMS_{signal}}{RMS_{noise}}\right)$ to calculate SNR values, where RMS is the root mean square of signal or noise for window sizes calculated using 2 and 4.5 km/s moveout velocities (Figure 2). By following this procedure, we exclude possible unreliable dispersion measurements from the tomography input datasets.
2. The associated wavelength (λ) of the input dispersion measurements must be shorter than one-third of the inter-station distance (Δ) for the average phase velocities (Figure S4 in Supporting Information S1). Previous studies have mentioned unreliable measurements for $\Delta < 3\lambda$ (e.g., Bensen et al., 2007; Köhler et al., 2011).

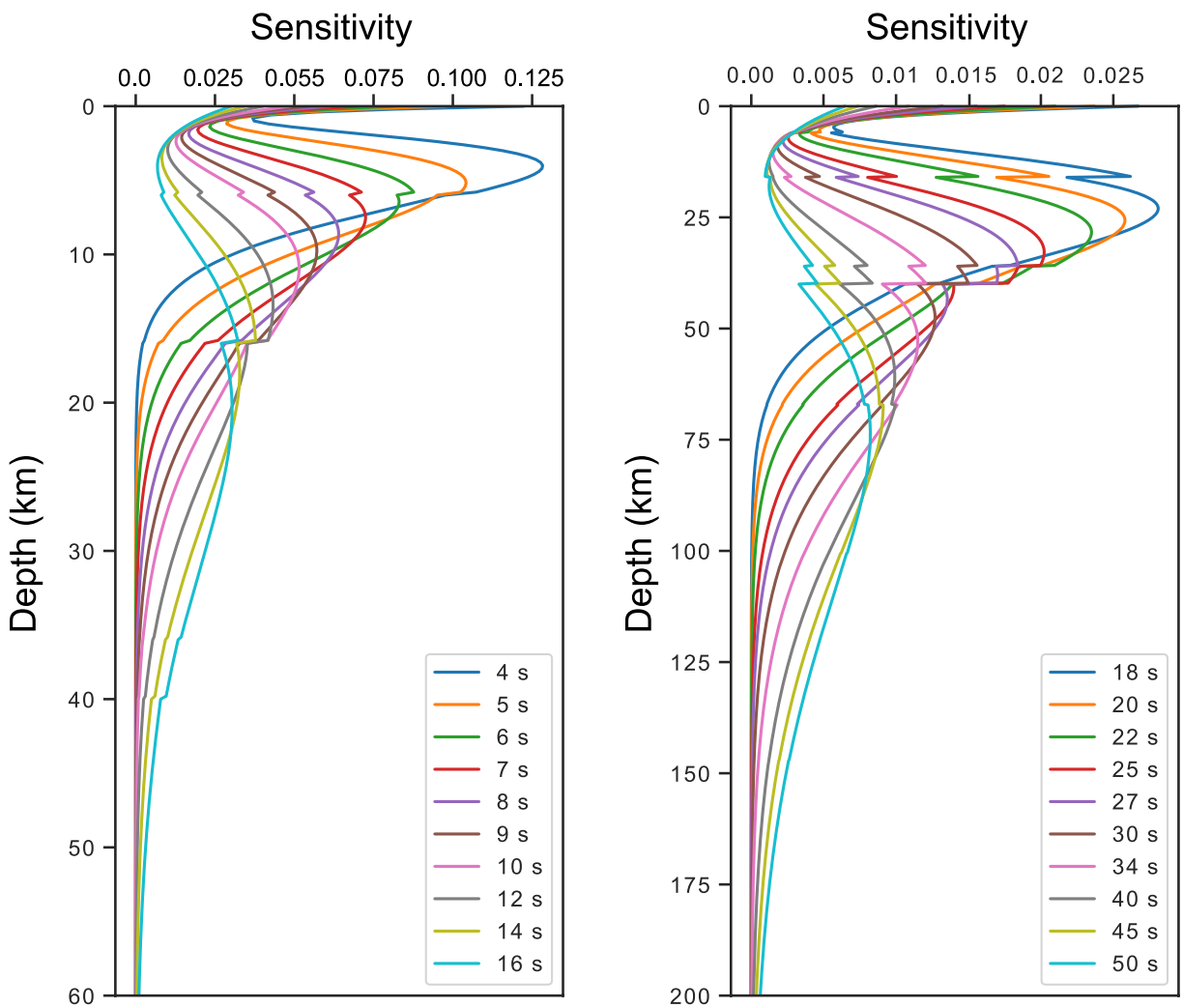

Figure 5. Fundamental mode Rayleigh wave depth sensitivity kernels for 20 periods used in this study. Note the difference between the axis ranges for these two subplots.

In addition to the above two criteria, the inversion procedure also includes an outlier exclusion step in which spurious paths are found based on the inversion misfit, and subsequently excluded from the final inversions. The proportion of paths excluded varies from 0 to 30% depending on period. After following the above procedure, we achieve a good azimuthal coverage for the input data used in the tomography. Due to the aperture of the study area, east-west directions (60°–120°) are the most common; however the full range of azimuths is covered and the selection criteria reduce bias (Figure S4 in Supporting Information S1).

2.4. Isotropic Shear Wave Velocity Inversion

In order to obtain shear velocity structure, we extracted local (1D) dispersion curves from 212 phase velocity map grid nodes, and inverted them for isotropic shear wave velocity profiles. Bathymetry information for all nodes was extracted from a global model (Amante & Eakins, 2009), and we fixed the water depth as the first layer in the inversion parameter file for the nodes located in water areas. The shear wave velocity models are then parameterized as one crustal layer and one mantle layer with 4 B-splines and 5 B-splines to describe velocity variations in the crust and mantle respectively. Crustal thickness solution in the inversions is an unknown parameter that was allowed to vary from 20 to 60 km. We set the maximum depth of inversions to 200 km that fully covers the sensitivity of even the longest period of the phase velocities in this study (i.e., 50 s; Figure 5). We used the inversion approach of Guo et al. (2016), a Bayesian inference method that outputs a joint probability density function (PDF)

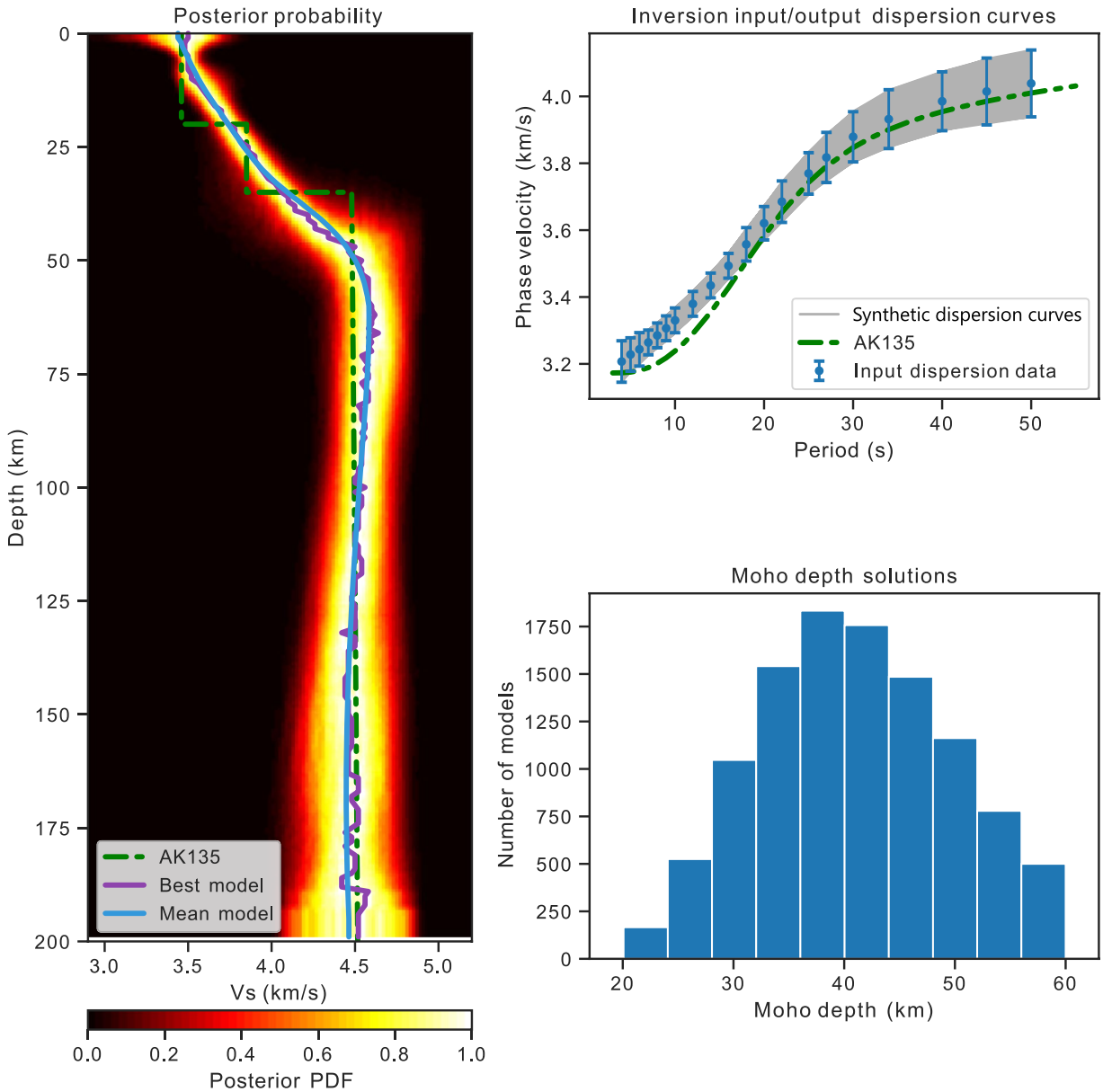

Figure 6. Shear velocity inversion results for the 1D average dispersion curve measured in this study. The left subplot illustrates the posterior probability density function for this inversion. The top right subplot shows the input dispersion curves, as well as the forward modeled dispersion curves for the accepted solutions. The bottom right subplot is the histogram for the accepted recovered Moho solutions. The shear wave and dispersion profile of the global reference model AK135 (Kennett et al., 1995) are drawn for comparison purpose (green dashed lines).

in the model and data space that contains the ensemble of accepted models, for which the synthetic dispersion curve matches the data within errors. The input data errors were assigned to the data as a fixed set of artificially chosen values in all 1D dispersion curves, typically increasing with increasing period and ranging from 0.0375 to 0.1 km/s. We checked the inversion results at all inversion nodes for stability and data fit within the selected range of errors. The posterior PDF is generated by data and updated prior information during the inversion process (Afonso et al., 2013; Tarantola, 2005). In this inverse problem scheme, due to parameter space being extremely large, a Markov Chain Monte Carlo (MCMC) sampling algorithm is adopted to sample the posterior distribution (Guo et al., 2016). As an example of the process, the regional average shear velocity profile resulting from the inversion of the 1D average dispersion curve is shown in Figure 6.

We construct our (pseudo) 3D shear wave velocity model by extracting and combining the mean profiles from the posterior PDF results. Although the model is parameterized to 200 km depth, we present our shear wave velocity model down to 60 km depth for which the shear velocity variations are best resolved. We interpolated the shear velocity data at each depth using a finer grid spacing of $0.15° \times 0.10°$ while applying a Gaussian smoothing function with the smoothing length of 50 km to remove lateral variations that are unrealistically small. The cross-section data are extracted from the interpolated shear velocity models at each depth by sampling the shear velocity model at every 5 km distance along the tracks.

Inspired by the method suggested by Kao et al. (2013), we estimated Moho depths at different locations by calculating the depths at which a certain percentage increase from typical crustal velocities (V_{crust}) toward typical mantle velocities (V_{mantle}) is reached in the 1D shear velocity profiles. Accordingly, V_{crust} and V_{mantle} at each location was calculated by taking the average from the velocities of each shear velocity profile at 15–25 and 55–65 km depths, respectively. To be consistent with the results by Kao et al. (2013), we obtained the results using the percentage increase values of 50% and 85%. However, after comparing the outcome with the results from previous receiver function studies (e.g., Darbyshire et al., 2017 and references therein), we decided to consider the average between the 50% and 85% solutions to construct the final Moho depth map in this study.

3. Model Resolution

We conducted various types of resolution tests at all periods and results for a subset of periods are presented in this article. The selection of representative periods was made to cover a wide range of depths and a variety of path coverage levels (Figure 5; Figures S1 and S2 in Supporting Information S1). We chose four periods: 6 s (best path coverage; sensitive to upper crustal depths), 14 s (average path coverage; sensitive to mid-crustal depths), 25 s (average path coverage; sensitive to lower crust and around Moho depths), and 40 s (low path coverage; sensitive to sub-Moho depths). All resolution tests were carried out following the same framework: generating a synthetic input phase velocity model, adding 0.02 km/s random noise, and inverting the measurements for an anisotropic phase velocity solution with the same path coverage and inversion parameters as that applied to the real data.

In this section, we explain the resolution test results for some spike tests (equivalent to the conventional checkerboard resolution tests in tomographic studies) that were designed based on custom geometric shapes and also a synthetic model based on the observed anomalous patterns in the final phase velocity maps (Figure 7). Results for more resolution test types including more spike tests (small-scale anomalies and stripe patterns; Figures S7 and S8 in Supporting Information S1), linear gradients (Figure S9 in Supporting Information S1), isotropic-anisotropic leakage tests (Figures S10 and S11 in Supporting Information S1), and rotated anisotropy tests (Figure S12 in Supporting Information S1) are also available in the Supporting Information S1.

1. Large hexagons with 320 km diameter (Figure 7, model A): Anomalies at all four representative periods are clearly recovered. The geometry of the hexagon centered at 72.5°W, 44°N is perfectly reproduced with almost no smearing effect. The other hexagons that are closer to the edges of the phase velocity maps show a minimal smearing effect at the hexagon edges that are the closest to the margins of the study area, which is expected given the density of crossing rays in those areas. Average amplitude recovery of synthetic anomalies at the selected periods varies between 60% and 75% with the best recovery for the two hexagons centered at 72.5°W, 44°N (New Hampshire), and 65°W, 45°N (Nova Scotia—New Brunswick), even at the longest periods (i.e., 40 s), compared to the others. Weak spurious anisotropy is observed in the margins of the study area, especially evident in the north and south in the 40 s map.
2. Small hexagons with 160 km diameter (Figure 7, model B): These small hexagon patterns have an edge size of 80 km, and are separated by ~160 km distance. The two anomalies located in the northeast of the study area near the Newfoundland coast are not recovered. The average amplitude recovery of the four anomalies in the center of the study area and the one over Nova Scotia varies between 45% and 65%, and their geometry is well recovered. The average amplitude recovery of other hexagons situated near the southern, western, and northern edges of the maps are in the 25%–55% range, but moderate to high smearing is observable due to insufficient path coverage beneath these areas. Comparing the anomalies in the northern edge of the study area with those situated along the eastern edge of the maps, the amplitude recovery of the hexagons in the eastern edge is better. In general, smearing at the edge areas is present and this effect is similar along different edges

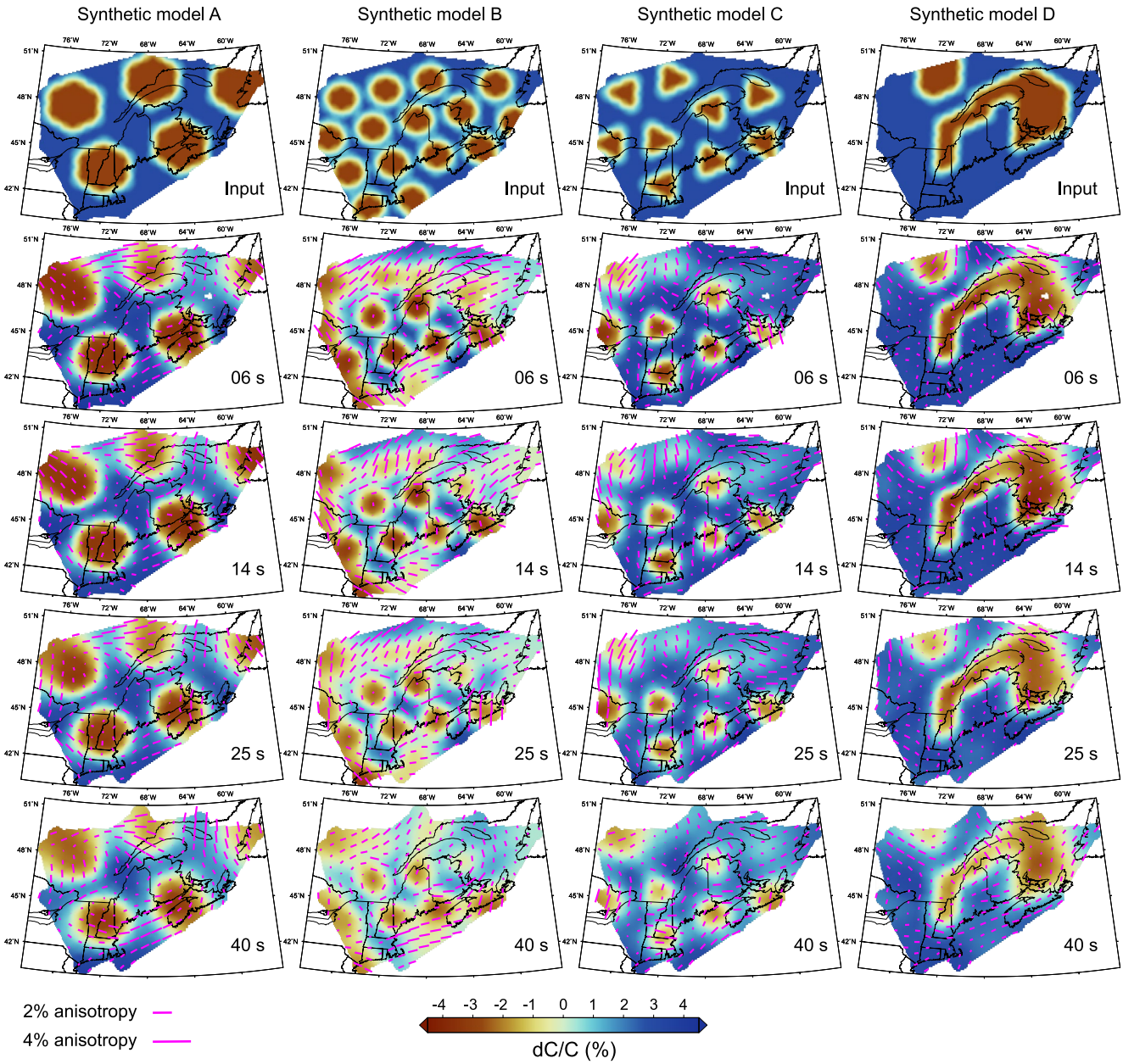

Figure 7. Structural resolution tests (spike tests) for the four representative periods (marked at the bottom right of each map). Results are shown for: (a) Large hexagons (320 km diameter). (b) Small hexagons (160 km diameter). (c) Small triangles (160 km edges). (d) Structure based on tomography results.

of the maps. Spurious anisotropy is less than ~0.5% in the center, but this effect is relatively larger at the edge areas (~1% to 1.5%), especially in the north, in Nova Scotia, and the southeastern edge.

3. Small triangles with 160 km edges (Figure 7, model C): These triangles are approximately the size of the average station spacing, and the smallest spike patterns that we tested in this study. The triangles are separated by ~240 km on average. Despite being very small features, the majority of the anomalies located in Nova Scotia, northern New Brunswick, NE USA (SE Maine, Massachusetts—New Hampshire), southern Quebec, and eastern Ontario are accurately reproduced with an average amplitude recovery of ~50% at the representative periods. Similar to the "small hexagons" tests, anomalies in the far northeast of the maps are not recovered. Although our tests suggest that the anomaly in the north, centered at 71°W, 49.5°N, has a relatively smaller average amplitude recovery of ~40%, this anomaly is still detectable. In this test, small spurious anisotropy of ~1% is observable in Nova Scotia and at the NW edge of the study area.

4. Based on the observed slow anomaly patterns in the final phase velocity maps, we created a synthetic input model for our study region (Figure 7, model D). The geometry of the anomalies in this test is recovered very well throughout the maps at different periods and the average amplitude recovery ranges from 65% to 85%. Even in the northeast of the Gulf of St. Lawrence, and in the north where other tests fail or have difficulty recovering the synthetic input anomalies, this test suggests that the main observed patterns in the final phase velocity maps are robust model features. Amplitude recovery gets less robust at longer periods; however, all anomalies stay detectable at all periods. The outer edges of the anomalies in the northeast and the north of the maps are more smeared due to a more limited path coverage in these areas. Spurious anisotropy in the north and northeast of the study area is also observable in this test
5. Other resolution tests are also available in the Supporting Information S1 (Figures S7–S12 in Supporting Information S1). We provide a very brief summary of those results here and readers are referred to the supporting information document for a more detailed discussion. The stripe pattern resolution tests are available in two directions: stripes along NE-SW (models S1 and S2; Figure S8 in Supporting Information S1), as well as stripes with NW-SE direction (models S3 and S4). These tests are presented for two different width configurations (240 and 80 km), and our analysis suggests that the average amplitude recovery is in the 55%–75% range at different periods (Figure S8 in Supporting Information S1). The results from 80 km width stripe tests along with single- and double-node tests in Supporting Information S1 (synthetic models E and F, Figure S7 in Supporting Information S1) suggest that the minimum resolvable length scale of structures in our study area is ∼80 km. The next tests are the linear gradient patterns that are conducted for two different directions (models G1 and G2; Figure S9 in Supporting Information S1). These tests are useful to investigate the bias due to a dominant number of paths along a specific direction. The linear gradient model G1 (i.e., along NW-SE direction) is better recovered than the model G2 (i.e., along NE-SW direction), especially at the longest periods (25–40 s). Due to the trade-off between isotropic and anisotropic structure, leakage between the isotropic and anisotropic components exists in the inversion of surface wave velocity. This may result in a non-robust feature looking robust (or vice versa), and therefore overinterpreting the results. Hence we tested this effect by only inputting one component of the model as the synthetic model (isotropic or 2ψ or 4ψ), and recovering the models to investigate the leakage effect (Figures S11 and S12 in Supporting Information S1). The results for this test suggest a very small leakage between the surface wave components. Finally, to investigate the robustness of our anisotropy models, we rotated the 2ψ anisotropy results by 90° and used them as input synthetic models at each period to be inverted and checked for the recovery level (Figure S13 in Supporting Information S1). The results of this test also suggests that our anisotropy results are reliable overall.

4. Results

4.1. Phase Velocity Model

The final phase velocity maps and maps of ray coverage at a selection of periods from 5 to 40 s are shown in Figure 8. Full sets of phase velocity maps and raypaths are available in Supporting Information S1 (Figures S1, S13 and S14 in Supporting Information S1). As discussed in Section 2.3, we invert the inter-station dispersion datasets for isotropic, 2ψ, and 4ψ components. However, we only interpret the maps of isotropic and 2ψ components, as the 4ψ component is not well constrained by the data and it is typically small. Only robustly resolved anisotropy results are shown on the final phase velocity maps. See Supporting Information S1 for explanation of this process.

Rayleigh wave phase velocity variations at each period give integrated shear velocity information over a depth range explained by depth sensitivity kernels (Figure 5). We use these kernels to understand the sensitivity of the phase velocity maps to the subsurface structure at different depths.

At short periods, 4–12 s, Rayleigh waves are predominantly sensitive to upper crustal depths (<∼15 km). We observe ±5% perturbations of phase velocities relative to the regional average at these periods. In contrast to the eastern Grenville and the SE Superior, the northern Appalachians are dominated by generally slower than average phase velocities. Slow anomalies are observed across the Gulf of St. Lawrence (GSL), Bay of Fundy (BOF), Gaspé Peninsula, along the St. Lawrence River, and beneath the Gulf of Maine (GME). In the easternmost study area, a slightly faster upper crust in Meguma than Avalonia is recovered. Almost the whole of Ganderia is dominated by slower than regional average phase velocities, except for a small fast anomaly that is observable close to

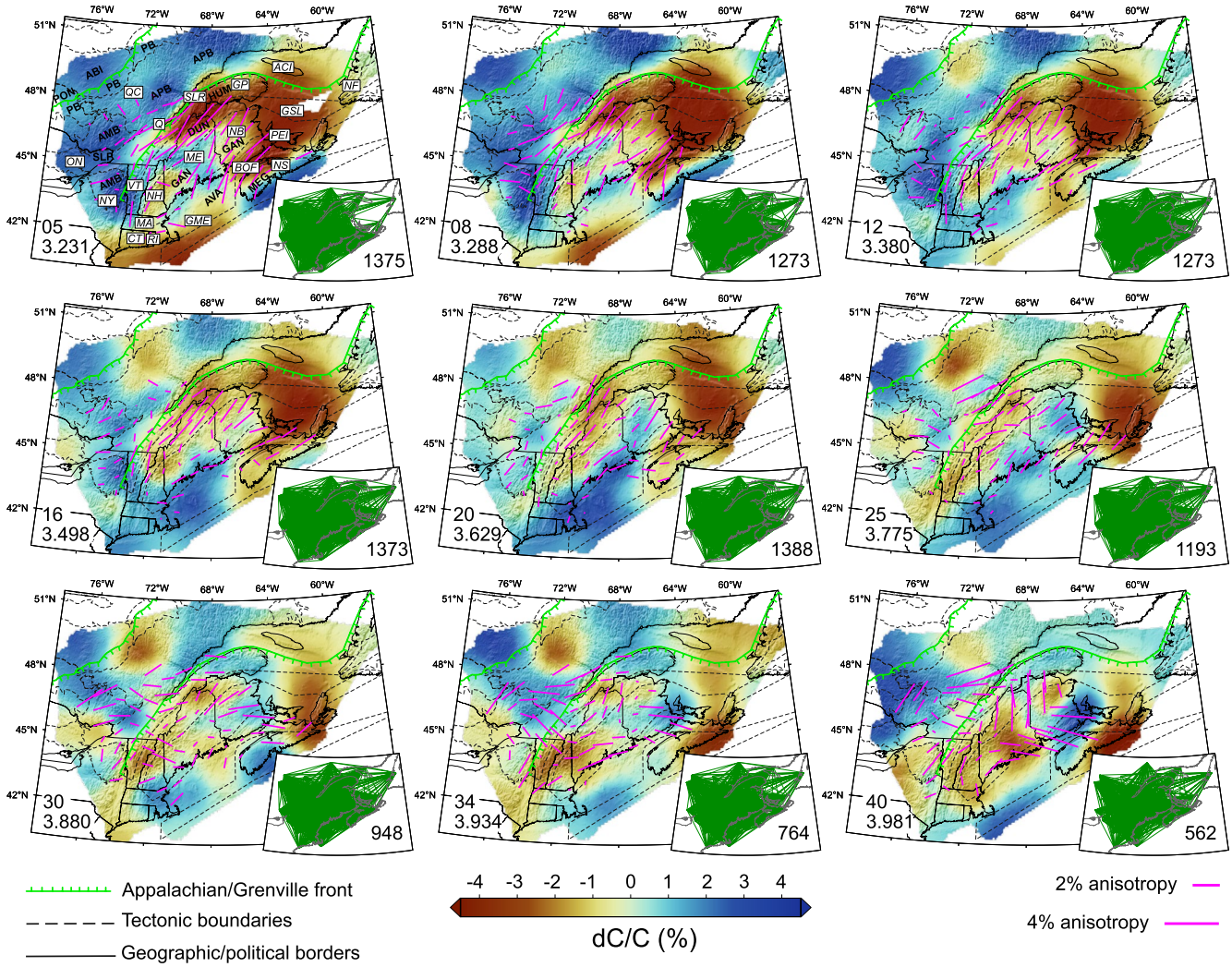

Figure 8. Final phase velocity maps and corresponding raypath coverage (small maps at the bottom right corner of the phase velocity maps; the number at bottom right is the number of rays) for a subset of periods in this study. The magenta bars represent the 2ψ anisotropy variations. The two numbers at the bottom left corner of the maps denote the period (s) and average phase velocity (km/s) respectively. Acronyms are explained in Figure 1.

the coastline in the west of BOF. Phase velocities of the Humber margin and the Dunnage zone are generally very similar in the northern Appalachians. Phase velocities in the Grenville Province are generally faster than average at short periods (2%–3% perturbation), with the exception of a weak slow anomaly located near the northwestern edge of the study area that is visible at periods >9 s (~1% perturbation). Our models suggest that the sampled part of the Superior Province in the northwest is dominated by fast phase velocities at short periods (maximum ~3% perturbation). A relatively small and weak slow anomaly in the northwest of the study area (periods > 10 s), and also a small region to the west of the Appalachian front along the St. Lawrence River are observed.

At intermediate periods, 14–20 s, the maximum sensitivities are to mid-crustal depths from ~15 to ~25 km (Figure 5). The observed anomalies in the phase velocity maps at these periods are generally weaker than those observed at periods sensitive to upper and lower crustal depths (~±3%). The slow anomaly in GSL is less strong at the intermediate periods compared to the short periods. We observe a fast structure (~2% anomaly) beneath GME, and this feature extends to the northeast crosscutting the three easternmost domains (Meguma, Avalonia, and Ganderia) at longer periods (18–20 s). The Humber and Dunnage zones are dominated by slow anomalies, and the Grenville and Superior are generally faster than the Appalachian domains. In the Grenville, we observe a prominent localized slow anomaly (~2%) situated in the northwest of the study area. A localized faster zone is also observed beneath the AMB zones in the Grenville Province.

At longer periods, 22–34 s, phase velocities have their maximum sensitivities to lower crust and around the Moho depths (25–45 km). At these periods, we observe ∼±4% phase velocity perturbations from the regional average. The NE-trending fast anomaly crosscutting the three easternmost tectonic domains is a striking feature at 20–25 s, though it becomes less continuous at longer periods. A slow anomaly located in BOF extends into the central part of this NE-trending anomaly at 30–34 s periods. The Dunnage zone and Humber margin are dominated by prominent slow anomalies (∼1%–2%). A strong slow anomaly of 3%–4% is observed beneath GSL. Fast anomalies in the Appalachians are observed beneath New Brunswick and southern PEI (27–34 s), and also under Gaspé Peninsula (30–34 s). In the Grenville, the SLP zone is dominated by slow velocities at 22–34 s. The AMB zone at these periods is also faster than the other regions in this orogen. The slow anomaly in the northwest of the study area is still a prominent feature, whereas the Superior province is ∼2% faster than the regional average.

The longest periods in this study (>34 s) are mostly sensitive to the depths around the Moho and uppermost mantle (45–60 km). With respect to the regional average velocities, we observe ∼±4% variations across the study area at these periods. Fast anomalies (2%–3%) in the Appalachians are observed beneath the GME and southern Maine, under New Brunswick, SW GSL and southern PEI, and southern Nova Scotia (∼3%). Most of the Humber and Dunnage zones are dominated by slow anomalies with 1%–2% strength at the longest periods, except for a ∼1% fast anomaly observed in Gaspé Peninsula at 34–40 s, as well as a fast anomaly observed south of Quebec City at 50 s. In the Grenville orogen, the slow anomaly in the northwest gets weaker at periods longer than 34 s and it is eventually replaced by a 1%–2% fast anomaly at 45 s (Figure S14 in Supporting Information S1). While the AMB zone in the north (76°W, 46.5°N) is recovered as a fast anomaly, the AMB zone in the south (in New York) is dominated by 1%–2% slower than average velocities at 40–50 s. The Superior craton is recovered as a relatively fast (∼2%) anomaly at the longest periods (e.g., 40 s).

In terms of 2ψ anisotropy variations, weak to moderate anisotropy of ∼1%–3% is observed across the study area at different periods. Overall, a ∼0.5%–1% stronger anisotropy is observed in the Appalachians than the Grenville province at periods <16 s. The predominant directions of the recovered anisotropy variations are typically along the general tectonic trend (i.e., NE-SW). We notice a change in the direction of anisotropy when comparing the results for the Appalachian and the Grenville domains on either side of the Appalachian structural front, especially near the SLP. According to our resolution tests (e.g., synthetic model D in Figure 7), it is unlikely that this change in the direction of anisotropy is an inversion artifact and this may provide further evidence for structural variation across the Appalachian front. Across eastern New Brunswick where a strong fast anomaly is observable at the longest periods (>30 s), the anisotropy variations are recovered as E-W to SE-NW orientations.

4.2. Shear Velocity Model

As discussed in Section 2.4, we construct our 3D shear velocity model from the inversion results of the extracted 1D dispersion curves. The maps of shear velocity variations at different depths are presented in Figure 9 (see also Figures S15–S17 in Supporting Information S1). To gain more perspective from the shear velocity model, we have also made cross-sections crosscutting different tectonic domains in the study area (Figure 10).

At upper crustal depths (<15 km), our shear velocity model shows a considerable range of variations from 3.2 to 3.75 km/s. The observed pattern of variations in the shear velocity model at these depths follows the geographical distribution of the units including various tectonic terranes and sedimentary basins. Similar to the observations of phase velocities, we notice that the SE Superior and the eastern Grenville Province have generally faster upper crustal structure than the northern Appalachians. In the Appalachians, localized fast velocity anomalies are observed in ∼10–15 km depth maps under southern Nova Scotia (Meguma), across GME (Avalonia), and the southwestern part of the Humber and Dunnage zones. The strongest slow anomalies (<3.4 km/s) are recovered at the shallowest depths (<10 km) beneath the GSL extending into BOF, under GP and NE St. Lawrence River, and in the far south of the study area beneath the GME. The thickness of these slow anomalies varies from 8–10 km beneath the GSL, to 5–6 km beneath the GP and NE St. Lawrence River, and ∼3–4 km under the BOF and in the extreme south of the study area in the GME. A similarly strong slow anomaly is also recovered at depths <∼3 km beneath the SLP in the Grenville Province (Figure 10-DD'; Figure S15 in Supporting Information S1). In general, the velocity structure of the upper crust beneath the eastern Grenville and the SE Superior does not appear to be as complex as the northern Appalachians, but our model suggests a clearly heterogenous structure beneath

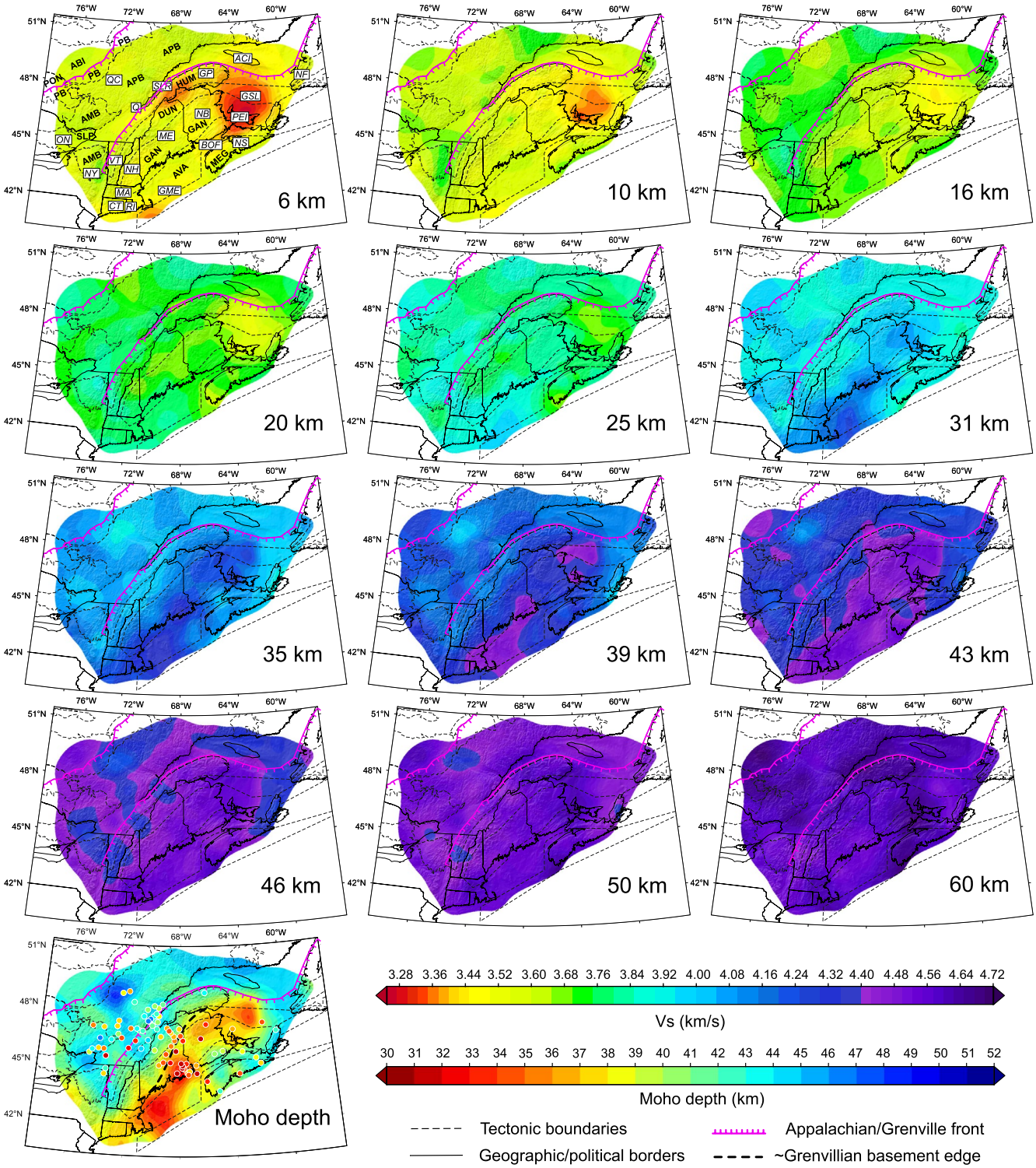

Figure 9. Final shear wave velocity maps at different depths. The map at the bottom left illustrates our Moho depth using the average of 50% and 85% velocity increase proxies (see text for more information). The scatter points on this map are the Moho estimates from previous studies (only a subset of their results are shown here; circles: Darbyshire et al., 2017 and references therein, diamonds: Li et al., 2018, squares: Shen and Ritzwoller 2016). See supporting information document for extra Moho depth maps estimated using different proxies (Figure S19 in Supporting Information S1) and also additional shear velocity maps (Figures S15–S17 in Supporting Information S1). Acronyms are explained in Figure 1.

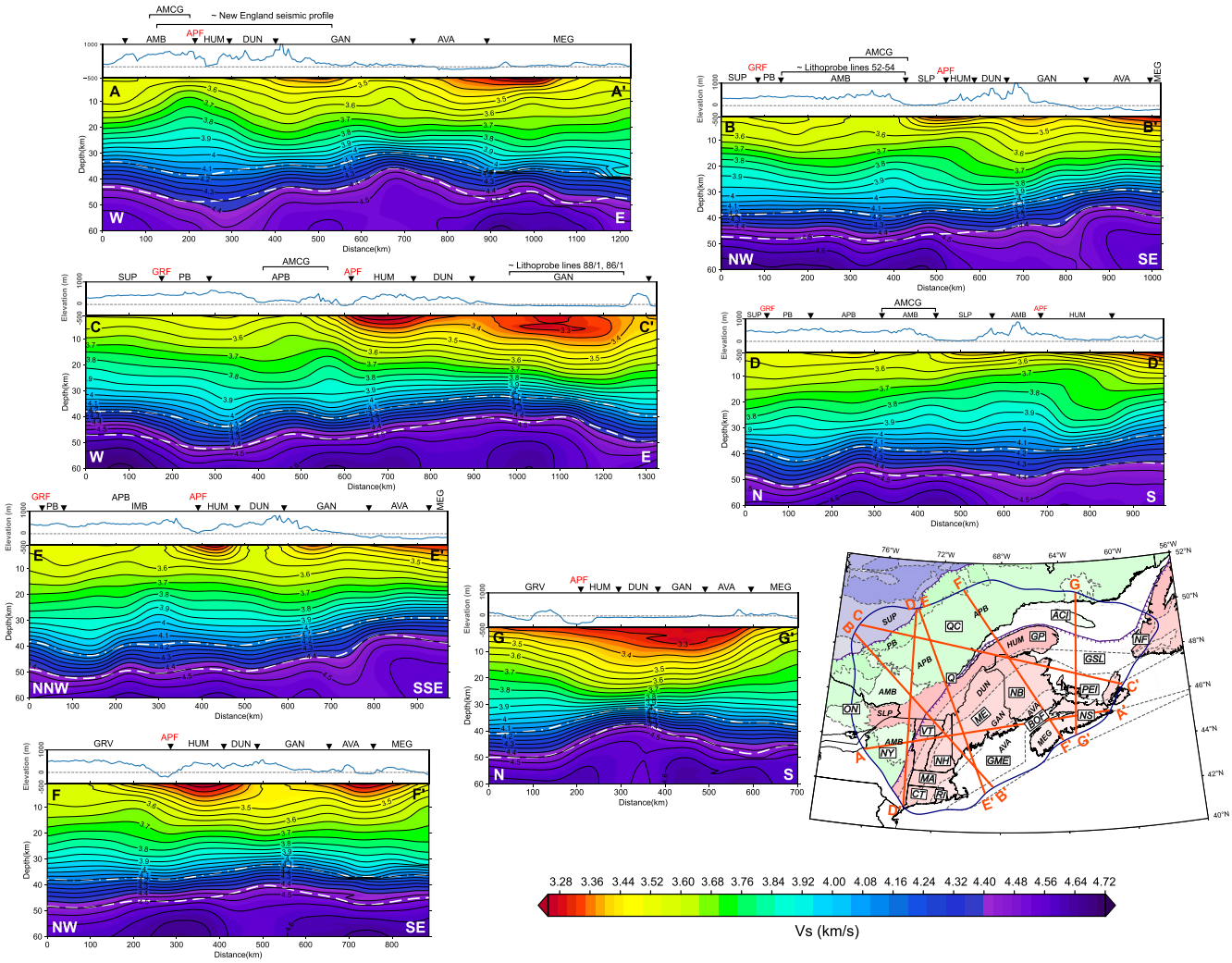

Figure 10. Cross-sections from the final 3D shear wave velocity model along five different profiles. The map at the bottom right denotes the location of the profile tracks. Our inferred Moho depths using the average of 50% and 85% velocity increase proxies are shown by the dashed white lines in the illustrations. Land elevation/water depth for each profile is shown above the velocity models. SUP: Superior, AMCG: anorthosite-mangerite-charnockite-granite, IMB: Interior Magmatic Belt, other acronyms are explained in Figure 1. Vertical axis of the velocity profiles is six times exaggerated.

these regions. Faster regions at this depth range are observed beneath the SE Superior Province, the southern AMB domain (in New York), and in the north of the study area. A relatively slow anomaly is observed at depths >12 km in the northwest of the study area. We also observe a velocity contrast across the Appalachian front, with higher velocities observable on the Grenville side at upper crustal depths (e.g., 13 km, Figure S15 in Supporting Information S1). Our shear velocity model does not distinguish the Grenville Province from the Superior craton at depths <10 km, but a systematically faster Superior is recovered at the deeper depths covered by this study.

At intermediate crustal depths (15–25 km), shear velocities in our study area vary between ~3.5 and 4.0 km/s suggesting significant variations in relative thickness of upper crust to lower crust (Figures 9 and 10). At these depths, fast regions include GME, western SLP and the southern AMB zone, and the Superior Province. Slowest regions at these depths are recovered beneath the GSL, central Ganderia domain, and the far SE of Nova Scotia. We note a velocity contrast occurring across the Appalachian front at intermediate crustal depths with slightly higher velocities (~0.05 km/s) beneath the Grenville Province than the Appalachians. Investigating the shear velocity model at depths from 25 to 45 km, we observe velocity variations in ~3.75–4.50 km/s range. This relatively wide range of shear velocity variations include both typical crustal and mantle velocities suggesting that the crust-mantle boundary in many regions of our study is likely situated within these depths. The observable fast regions in the Appalachians follow a SW-NE trend covering GME, southern Maine, New Brunswick, and the

southwestern GSL crosscutting the three Appalachian coastal domains. Parallel to this fast anomaly to the north, our shear wave velocities are 0.1–0.2 km/s lower indicating a strong velocity contrast occurring near the Gander-ia-Dunnage boundary. Further northwest, crossing the Appalachian front, we observe a small increase of shear wave velocities at depths >∼30 km on the Grenville side. Maps of shear wave velocities at lower crust to Moho depths (25–45 km) are indicative of heterogenous eastern Grenville seismic structure. A striking slow anomaly in the NW of the study area is observed with velocities < 4.4 km/s at 35–50 km depths. We also observe a weaker slow anomaly centered beneath the western SLP and expanding toward the AMB zones in the Grenville Province at these depths. Although differences in data coverage make it difficult to compare seismic structures equally at all regions sampled, a general increase of shear velocity with age is observable for the first order tectonic domains at mantle depths (Superior > Grenville > Appalachians; Figure S18 in Supporting Information S1). One exception is the uppermost mantle structure beneath southern New Brunswick and southwestern Nova Scotia that is considerably (∼0.2 km/s) faster than other tectonic domains of the Appalachians.

The cross-section illustrations provide evidence for a very complex 3D crustal velocity structure beneath the study area (Figure 10). The prominent shallow low-velocity zones (<3.4 km/s) beneath the southern GSL (profiles CC', GG'), Bay of Fundy (profiles AA', FF'), Gulf of Maine (profiles BB', EE'), St. Lawrence river (profiles CC', EE', FF'), and St. Lawrence Platform (profiles BB', DD') have very different thicknesses from less than 3 km to a maximum of 10 km. Near the major surface tectonic boundaries (i.e., Appalachian/Grenville fronts), our cross-section illustrations suggest significant lateral heterogeneities at all depths covered by this study. The Moho depth variations from the two shown proxies across different tectonic domains indicate that the crustal thickness can be highly variable over a short distance (e.g., profiles EE', GG'; ∼10 km variations over ∼100 km distance).

5. Discussion

Although ambient noise tomography is inherently insensitive to fine stratigraphic details, our models reveal unprecedented details of the crust and sub-Moho structure beneath the study area. This enables us to discuss the observed features in terms of their tectonic implications. We note that due to the highly nonlinear relationship between the lithology and seismic velocities (e.g., Fountain & Christensen, 1989), we have been careful to not interpret the results in terms of variations in lithology. That said, our resolution analyses suggest that the variations of seismic velocities at the scale of tectonic zones and subprovinces are well constrained.

5.1. Thickness of the Sedimentary Layers

According to depth sensitivity kernels and the shortest periods covered by this study (Figure 5), we should be able to resolve the geometry of the sedimentary layers with thickness >∼3 km. In our 3D model, shear velocities lower than ∼3.4 km/s are interpreted as sedimentary layers. Accordingly, the thickest sedimentary layer in our study area is located beneath the GSL and PEI (Figures 9 and 10) with a thickness of ∼8–10 km. This sedimentary basin has a U-shaped geometry with the maximum thickness located beneath PEI. Our interpretations are consistent with the previous ANT study carried out over the GSL (Kuponiyi et al., 2017). The next thickest sedimentary layer is located under the NE St. Lawrence River and beneath the Humber margin with a thickness of ∼5–6 km. This sedimentary layer was developed after break-up of Rodinia at ∼615 Ma which resulted in producing extensional features including failed rift arms of the St. Lawrence (e.g., Kamo et al., 1989, 1995). Across the BOF, thickness of the sedimentary layer is likely to be ∼3–4 km. Although our shear velocities are not best constrained at depths <3 km, we note that the thickness of the sedimentary layer may be ∼1–2 km beneath the eastern SLP.

5.2. Crust-Mantle Boundary

Variations in our Moho depth map agree well with the results from previous studies that used receiver function techniques and joint inversion of surface waves and receiver functions (Figure 9). Due to the nature of the depth sensitivity kernels (Figure 5), surface wave techniques are relatively insensitive to sharp discontinuities, resulting in models with a transitional crust-mantle boundary. However, as discussed by previous authors (e.g., Kao et al., 2013), implementing proxies defined as a certain increase from typical crustal velocities to typical mantle velocities enables us to have acceptable estimates for Moho depths, as well as relative variations of Moho

thickness across the study area (Figure S19 in Supporting Information S1). We note that eclogitization processes that may have occurred in the past at lower crustal depths in the study area could result in underestimating Moho depths from our velocity models.

The Grenville Province and the northern Appalachians have experienced different tectonic formation and evolution mechanisms, including their temperature regime, the spatial scale of the terranes involved in the orogenesis and the duration of accretion and collision. This difference is clearly manifested in our Moho depth estimates derived from the 3D shear velocity model. The crust beneath the Grenville orogen is typically thicker than the Appalachian province (except for Nova Scotia and southern New Brunswick). Average crustal thickness resolved by our Moho proxy of choice in the Grenville orogen is ~40–45 km, which is consistent with the estimates from previous seismic studies (Figure 9; Darbyshire et al., 2017; Li et al., 2018; Shen & Ritzwoller, 2016 and references therein). The deepest crust-mantle transition (>50 km) occurs in the northwest of the study area, centered at 73°W, 49°N, in the Grenville Province (Figure 10, profile CC'). This localized feature is coincident with a negative Bouguer gravity anomaly in southeastern Canada (e.g., Ludden & Hynes, 2000). Interpretation of the Lithoprobe seismic profiles also suggests a thicker crust within the southern vicinity of the Grenville front (Martignole & Calvert, 1996). While our results suggest a thick crust beneath this region, results from previous receiver functions suggest a relatively shallower Moho (Figure 9). This anomalously thick crust is situated between the Allochthon Boundary Thrust (ABT, the boundary between PB and APB at the surface; Figure 10, profile EE'; e.g., Rivers, 2015) and Interior Magmatic Belt (IMB, located in central Grenville, marking the northern limit of post-Grenville magmatism; e.g., Hynes & Rivers, 2010). Thus the location of this feature suggests that it likely formed during or before the Grenvillian orogenic phases. A thicker crust than the average in the Grenville is also suggested beneath the younger SLP and the western AMB zones (45–50 km; Figure 9).

Crustal thickness variations across internal tectonic boundaries of the Appalachians do not seem to have clear systematic signatures. They rather suggest a very complex geometry manifested in significant heterogeneity within tectonic domains. While a generally shallower Moho is suggested beneath Ganderia compared to other tectonic domains of the Appalachians, the thinnest crust in our study area is observed beneath Gulf of Maine (Avalonia) and Gulf of St. Lawrence (Dunnage zone; Figures 9 and 10, profile EE'). We suggest a ~40–45 km crustal thickness beneath southern Nova Scotia, very similar to the suggested Moho depths beneath the Grenville orogen. A relatively large difference between our Moho proxies suggests that the Moho discontinuity beneath this area is likely to be a gradual interface (Figure 10, profile FF'; Figure S19 in Supporting Information S1). In the same region, receiver function measurements suggest a significantly thinner crust (30–40 km; Darbyshire et al., 2017 and references therein). Although the results from a surface wave study cannot be directly compared to results from receiver functions due to the inherent differences in their methods, the mismatch between our inferred Moho depths and the results from previous receiver function studies for southern Nova Scotia suggests a complex crust-mantle transition beneath this region.

Some of our cross-sections are constructed along previously conducted active seismic profiles in our study area, and the results are generally in good agreement (Figure 10, profiles AA', BB', CC'). The New England seismic refraction/wide-angle reflection survey was conducted in the late 1980s, and crosscuts four USA states from west to east: New York, Vermont, New Hampshire, and Maine (Hughes & Luetgert, 1991). It included both the Grenville and Appalachian Provinces and imaged a complex multi-layer crustal structure in the Appalachian terranes, an eastward dipping Grenvillian basement under the Appalachians, and a progressively shallower Moho beneath the Appalachian orogen. These findings are consistent with our observations in shear velocity profile AA'. The locations of Lithoprobe lines 52–54 coincide with a portion of shear velocity profile BB'. Noteworthy observations are a complex and laterally heterogeneous seismic structure beneath this region with variable Moho depth geometry, and extension of Parautochthonous Archean basement to more than 200 km southeast of the Grenville front reaching the Moho (Ludden & Hynes, 2000). The Lithoprobe reflection-refraction lines 86/1–88/1 in southern GSL infer an increase in crustal thickness toward northeastern Nova Scotia (Hall et al., 1998), which is similar to the geometry suggested by our shear velocity model beneath this region (profile CC').

Previous receiver function studies have noted a sharp Moho offset occurring within a narrow zone in the central northern Appalachians, interpreted as the boundary separating the Laurentian (Grenvillian basement) and Gondwanan units at depth (Li et al., 2018, 2020). A supporting evidence for this interpretation is that this NE-SW trending Moho contrast feature is very well correlated with the trend of Peri-Gondwanan magmatic arc assemblages in Ganderia at the surface (e.g., Macdonald et al., 2014). Our maps of shear velocities and Moho

estimates are consistent with this interpretation, and a step-like Moho geometry near the Ganderia-Dunnage boundary is suggested. The geometry of this feature in our model does not perfectly follow the surface tectonic boundaries, however. Instead, we suggest an oblique geometry (relative to the average NE-SW tectonic trend) for the eastern edge of the Grenvillian basement beneath the Appalachians. In the northeast, the eastern edge of the Grenvillian basement is likely located in the south of the Gaspé Peninsula near the Humber-Dunnage surface boundary, whereas it occurs within Ganderia in the southwest. This observation supports the view that Laurentia may have experienced a variable orogenic (or post-orogenic) modification along its eastern edge in the northern Appalachians (Li et al., 2020).

5.3. Crustal Anistropic Fabrics

The past tectonic events in our study area may have overprinted older orogenic trends at different depths. Our period-dependent 2ψ anisotropy results can be interpreted in terms of deformations due to past tectonics. In particular, significant variations of anisotropy magnitude and/or direction with period, as well as variations over a short distance are investigated. We note that the resolution of our anisotropy results is much lower than the isotropic component. We therefore limit our interpretation of the anisotropy results to areas where a decent azimuthal coverage is provided by the inter-station dispersion datasets. For example, the anisotropy beneath the central part of our study area across the Appalachian front, southeastern Nova Scotia and beneath the Bay of Fundy are likely well-constrained, whereas limited azimuthal coverage over the GSL does not permit us to include this region in our interpretations (Figure S3 in Supporting Information S1).

As discussed in Section 4.1, the dominant direction of anisotropy generally follows the geological trend. That said, interesting short scale variations of anisotropy are observable in different regions at different periods. For example, we observe localized variations of anisotropy, likely related to Mesozoic rifting, in Bay of Fundy manifested by a change in the direction of anisotropy, from NE-SW to E-W and SE-NW orientations, at intermediate to longest periods of this study. Previous shear wave splitting results suggested an ESE-WNW to WSW-ENE fast direction with a large splitting time ($\delta t > 1$ s) that requires a plate-scale anisotropic layer spanning both the crust and mantle beneath this area (Gilligan et al., 2016). While our model supports this interpretation, we note E-W anisotropy orientations with strong anisotropy beneath southern Nova Scotia and New Brunswick at periods sensitive to lower crust and lithospheric uppermost mantle depths. A westward (present-day coordinates) flat subduction of the Acadian lithosphere may have overprinted the crustal anisotropic fabric in the Middle Paleozoic (Bagherpur Mojaver et al., 2021).

We note a change in the dominant direction of anisotropy across the Appalachian front beneath the eastern AMB and SLP domains that is mainly evident at periods mostly sensitive to mid-to-lower crustal depths, between 7 and 27 s. While the direction of 2ψ anisotropy on the Appalachian side of this boundary is generally parallel to the main tectonic trend, the anisotropy directions in the SE Grenville orogen are almost perpendicular to this orientation. The maps of azimuthal coverage and our resolution analysis suggest that the 2ψ variations beneath this region are well constrained (Figures S3, S10–S12 in Supporting Information S1). Results from previous shear wave splitting studies also suggest a similar E-W fast axes orientation near the Appalachian front (e.g., Darbyshire et al., 2015). Surface geology corresponds to the mafic Adirondack terrane containing anorthosite massifs dated between 1.1 and 1.3 Ga (Rivers et al., 1989). This age pre-dates the Grenville orogenesis suggesting that maybe the observed E-W direction of anisotropy is a pre-Grenvillian fossil crustal fabric that has remained intact. Alternatively, it is also possible that thermal and melt weakening due to the rise of asthenosphere after delamination of the lithosphere beneath the orogenic lid caused lateral flow of the lower-mid crust modifying the crustal anisotropic fabric (the collapsed large hot orogen model; e.g., Rivers, 2015).

5.4. Tectonic Implications

Variations in the relative thickness of the lower crust and upper crust carry information about crustal evolution due to past tectonic processes (e.g., Brown, 2010). Comparing the Grenville and Appalachian provinces, the lower crustal layer (shear velocities in ~3.8–4.4 km/s range) beneath the Grenville orogen is generally thicker. This is especially evident in the western shear velocity sections (Figure 10, BB', CC', EE'). High velocity lower crust beneath the Grenville Province is consistent with protracted preservation of a partially eclogitized root at the base of the crust (Darbyshire et al., 2017 and references therein). A relatively thick and fast lower crust in the central

Grenville Province may also be marking the southeastern extent of the highly reflective Archean Parautochthon at lower crustal depths (Hynes & Rivers, 2010). This is compatible with the interpretation of Lithoprobe lines 52–54 that suggests the ABT reaches the Moho (Ludden & Hynes, 2000). Results from these reflection profiles suggest that the Superior craton continues as a wedge into the Grenville lower crust 200–300 km southeast of the Grenville front (Ludden & Hynes, 2000; Rivers, 1997).

The Grenville Province contains a significant amount of anorthosite with ages pre-dating the Grenvillian orogenic phases (Hynes & Rivers, 2010; Musacchio et al., 1997). It is suggested that Grenville lower crust in the Mid-Proterozoic was significantly modified by the emplacement of these mafic intrusive units (Musacchio et al., 1997). The signature of these events is also manifested in the present-day seismic structure of the Grenville crust by high V_p/V_s ratios (e.g., Levin et al., 2017), and high shear velocity lower crust (e.g., Petrescu et al., 2016). Our shear velocity model suggests that the anorthosite-mangerite-charnockite-granite (AMCG; Figure 10) complexes including anorthosites in the Adirondack mountains (Marcy Anorthosite; profile AA'; Musacchio et al., 1997), anorthosites in the Morin terrane (Morin Anorthosite; profiles BB', DD'; Martignole & Calvert, 1996), and the AMCG unit in the central APB domain (Lac St-Jean AMCG; profile CC'; Hynes & Rivers, 2010), all have higher seismic velocities than their surrounding terranes at upper crustal depths. Investigating our shear velocity cross-sections, it is also evident that these AMCG units are underlain by localized high shear velocities at lower crustal depths, as well as relatively thicker crust (Figure 10). However, the high velocity lower crust and deeper Moho signature of these features are not exactly beneath the surface AMCG units, and they are shifted toward the Appalachian front (e.g., profile CC', Figure 10). This may provide evidence for ductility of middle and lower Grenville crust during or after the orogenic phases. A thicker crust beneath these regions is also coincident with a thicker Moho interface (Figure S19 in Supporting Information S1) which can be explained by underplating processes (Petrescu et al., 2016).

Comparing the shear velocity profiles perpendicular to the trend of the Appalachian tectonic domains along different parts of the orogen (Figure 10), it becomes clear that the 3D seismic structure of the northern Appalachian crust is very complex and more variable than that observed beneath the Grenville and the SE Superior. Previous seismic studies also mentioned a more complex Appalachian crust than the older tectonic provinces in eastern Canada as suggested by their Moho depth and Poisson's ratio variations (e.g., Darbyshire et al., 2017; Levin et al., 2017; Petrescu et al., 2016). Results from this study suggest changes of seismic signatures including crustal thickness, Moho thickness, and relative thickness of upper and lower crustal layers over a relatively short distance due to the diverse nature of tectonic events that resulted in the assembly of the Appalachians. Phase velocity maps from a previous regional-scale tomography study suggest that the structures at lower crust and uppermost mantle depths beneath the northern Appalachians are dominated by slower than average velocities compared to those of the Grenville and Superior Provinces (Petrescu et al., 2017). Thanks to a much higher data coverage in this study, we were able to show that localized high velocity regions also exist at these depths beneath the northern Appalachians (Maine, New Brunswick, and Nova Scotia).

A variable seismic structure of the crust within the Taconic terranes of the northern Appalachians provides evidence for at least two different metamorphism episodes with different characteristics that occurred during the Early Paleozoic Taconic orogeny. Beneath the St. Lawrence rifting system and the Humber margin, upper and middle crust under the first sedimentary layer is generally faster than its surroundings in the Appalachians and the Grenville in our shear velocity model (Figure S15 in Supporting Information S1). This region also coincides with high V_p/V_s ratios indicating a high mafic content (Petrescu et al., 2016). It is possible that rift-related tectonics after break-up of Rodinia not only resulted in development of a relatively thick sedimentary basin, but also created a zone of weakness in the crust acting as a stress guide for magmatic material which modified the composition of the crust beneath these regions. The observed higher velocity upper crust beneath these areas may be a result of different accretional/collisional processes that occurred in the evolution of the northern Appalachians during the Taconic orogeny. Accretion of the Humber margin to Laurentia was different in terms of rheological coupling between the upper and lower plates than the later arriving Peri-Laurentian terranes (i.e., Dashwoods, van Staal & Zagorevski, 2020). Deformation was limited to underthrusted Humber margin manifested in low grade metamorphism and structurally intact suprasubduction-zone ophiolites, whereas the adjacent Dashwoods block is dominated by strongly metamorphosed and deformed sedimentary rocks of various ages and arc ophiolites (van Staal & Zagorevski, 2020 and references therein). Accordingly, we suggest that the short scale variations of seismic

velocities within the Peri-Laurentian terranes of the Appalachians are mostly compositional and preserve evidence for variable degree of metamorphism at distinct accretionary/collisional episodes of the Taconic orogeny.

As suggested by our tomographic models (Figures 8 and 9), crustal structure of the Salinic terranes (i.e., Ganderia) is seismically slower and generally different than that of the later arriving Peri-Gondwanan terranes (i.e., Avalonia and Meguma). The differences are especially evident at lower-crustal to sub-Moho depths (25–45 km), likely due to a deeper Moho discontinuity and generally faster lower crust beneath composite Avalonia and Meguma than the Ganderia domain. Ganderia's rifting from West Gondwana, its drift across the Iapetus Ocean, and its accretion to Laurentia were independent from the Avalonia and Meguma terranes (van Staal et al., 2021). Hence after the onset of the Paleozoic, Ganderia and Avalonia were two different unrelated terranes (van Staal et al., 2009). As opposed to Ganderia, Avalonia was not involved in the Appalachian accretionary events until the Late Silurian (van Staal & Barr, 2012), and the observed differences of the seismic characteristics may be due to their different tectonic histories in the Early Paleozoic in terms of within-plate magmatism and metamorphism en route to Laurentia (van Staal et al., 2012). A lack of significant difference for the crustal seismic signatures of Avalonia and Meguma may also suggest that Avalonia and Meguma were never separated by a wide ocean basin. It is also likely that they were only separated by extended continental crust rather than an oceanic basin until they collided during the Neo-Acadian orogeny. This interpretation is also compatible with the observed relatively thick crust beneath the pertinent terranes.

6. Conclusions

Using more than 2 yr of ambient seismic noise data recorded by relatively dense arrays of broadband seismograph stations, we took the most detailed look at the seismic structure of the crust beneath SE Canada and the NE USA to date. Our Rayleigh wave tomographic models enabled us to discuss the observed variations in the azimuthal anisotropy, the crustal velocities, and the Moho depth and thickness in terms of their tectonic implications. The azimuthal anisotropy is oriented mainly along the general tectonic trend (i.e., NE-SW), but localized variations of seismic anisotropy are observed beneath the Bay of Fundy and across the Appalachian structural front. The Precambrian tectonic provinces, namely the Grenville and the Superior, are generally dominated by fast seismic velocities, whereas prominent slow velocity regions are observed beneath different regions in the Appalachians. Relatively thick sedimentary layers are observed beneath the Gulf of St. Lawrence, the St. Lawrence River, Bay of Fundy, and under the St. Lawrence Platform with their thicknesses interpreted to be 8–10, 5–6, 3–4, and 1–2 km, respectively. Using shear velocity proxies, we estimated Moho depth and thickness across the study area. Crustal thickness in the study area is highly variable, ranging from ~32–52 km. Regions with the deepest Moho are found beneath the Grenville Province, whereas the shallowest Moho areas are beneath the Gulf of Maine and the Gulf of St. Lawrence in the Appalachians. A thicker crust and Moho interface in the Grenville Province could be explained by underplating processes. A NE-SW trending Moho offset feature in the central northern Appalachians is interpreted as the boundary between the Peri-Laurentian and Peri-Gondwanan terranes at depth. Variations of seismic signature within the westernmost terranes of the Applachians (i.e., the Taconic terranes) provide evidence for at least two episodes of metamorphism in the Peri-Laurentian zones of the northern Appalachians. We observe very similar seismic signatures for Avalonia and Meguma, whereas the seismic velocities in the Peri-Gondwanan tectonic domains of Ganderia and Avalonia are notably different. Ganderia crust is generally seismically slow, whereas the post-Acadian domains of Avalonia and Meguma are dominated by fast velocities. These seismic signatures could suggest a difference in the tectonic history between the Ganderia and Avalonia-Meguma terranes in terms of their intra-plate magmatism and metamorphism as they moved toward Laurentia in the Early Paleozoic. Similar seismic signatures observed for Avalonia and Meguma, especially at mid-to-lower crustal depths, may suggest that they were originally separated by either a narrow ocean basin or by extended continental crust.

Data Availability Statement

The seismic data used in this study are archived at the IRIS Data Management Center (http://www.iris.edu/hq/; http://ds.iris.edu/ds/nodes/dmc/; networks [CN; Geological Survey of Canada, 1989], [NE; ASL, 1994], [TA; IRIS Transportable Array, 2003], [PO; Eaton et al., 2005], [X8, Y8; Menke et al., 2012; SEIS-UK, 2013]) or at

the Canadian National Data Center, Natural Resources Canada (https://earthquakescanada.nrcan.gc.ca/stndon/index-en.php; CN; Geological Survey of Canada, 1989).

Acknowledgments
The authors thank the editor and reviewers for their helpful comments, which improved the manuscript. We thank Hamzeh Sadeghisorkhani for sharing the dispersion calculation code, *GSpecDisp*, with us, Sergei Lebedev for permission to use the tomography code, and Zhen Guo for providing the depth-inversion code. We appreciate the work done by the operators of the six seismograph networks used in this study. All figures in this study were generated using Generic Mapping Tools (Wessel et al., 2013) and Python Matplotlib library (Hunter, 2007). This research was supported by the Natural Sciences and Engineering Research Council of Canada (NSERC/CRSNG) through its Discovery Grant and Canada Research Chair programs.

References

Afonso, J., Fullea, J., Griffin, W., Yang, Y., Jones, A., D. Connolly, J., & O'Reilly, S. (2013). 3-D multiobservable probabilistic inversion for the compositional and thermal structure of the lithosphere and upper mantle. I: A priori petrological information and geophysical observables. *Journal of Geophysical Research: Solid Earth*, *118*(5), 2586–2617. https://doi.org/10.1002/jgrb.50124

Amante, C., & Eakins, B. W. (2009). *ETOPO1 arc-minute global relief model: Procedures, data sources and analysis*. National Geophysical Data Center. https://doi.org/10.7289/V5C8276M

Albuquerque Seismological Laboratory (ASL)/USGS. (1994). New England Seismic Network. (Dataset). International Federation of Digital Seismograph Networks. https://doi.org/10.7914/SN/NE

Bagherpur Mojaver, O., Darbyshire, F., & Dave, R. (2021). Lithospheric structure and flat-slab subduction in the northern appalachians: Evidence from Rayleigh wave tomography. *Journal of Geophysical Research: Solid Earth*, *126*(4), e2020JB020924. https://doi.org/10.1029/2020JB020924

Bensen, G., Ritzwoller, M., Barmin, M., Levshin, A. L., Lin, F., Moschetti, M., & Yang, Y. (2007). Processing seismic ambient noise data to obtain reliable broad-band surface wave dispersion measurements. *Geophysical Journal International*, *169*(3), 1239–1260. https://doi.org/10.1111/j.1365-246X.2007.03374.x

Bensen, G., Ritzwoller, M., & Shapiro, N. M. (2008). Broadband ambient noise surface wave tomography across the United States. *Journal of Geophysical Research: Solid Earth*, *113*(B5). https://doi.org/10.1029/2007JB005248

Bensen, G., Ritzwoller, M., & Yang, Y. (2009). A 3-D shear velocity model of the crust and uppermost mantle beneath the United States from ambient seismic noise. *Geophysical Journal International*, *177*(3), 1177–1196. https://doi.org/10.1111/j.1365-246X.2009.04125.x

Boyce, A., Bastow, I., Darbyshire, F. A., Ellwood, A., Gilligan, A., Levin, V., & Menke, W. (2016). Subduction beneath Laurentia modified the eastern North American cratonic edge: Evidence from P wave and S wave tomography. *Journal of Geophysical Research: Solid Earth*, *121*(7), 5013–5030. https://doi.org/10.1002/2016JB012838

Brown, M. (2010). Melting of the continental crust during orogenesis: The thermal, rheological, and compositional consequences of melt transport from lower to upper continental crust. *Canadian Journal of Earth Sciences*, *47*(5), 655–694. https://doi.org/10.1139/E09-057

Carr, S., Easton, R., Jamieson, R. A., & Culshaw, N. (2000). Geologic transect across the Grenville orogen of Ontario and New York. *Canadian Journal of Earth Sciences*, *37*(2–3), 193–216. https://doi.org/10.1139/e99-074

Clouzet, P., Masson, Y., & Romanowicz, B. (2018). Box tomography: First application to the imaging of upper-mantle shear velocity and radial anisotropy structure beneath the north American continent. *Geophysical Journal International*, *213*(3), 1849–1875. https://doi.org/10.1093/gji/ggy078

Clowes, R. M. (2010). Initiation, development, and benefits of Lithoprobe—Shaping the direction of Earth science research in Canada and beyond. *Canadian Journal of Earth Sciences*, *47*(4), 291–314. https://doi.org/10.1139/E09-074

Cook, F. A., White, D. J., Jones, A. G., Eaton, D. W., Hall, J., & Clowes, R. M. (2010). How the crust meets the mantle: Lithoprobe perspectives on the Mohorovičić discontinuity and crust–mantle transition. *Canadian Journal of Earth Sciences*, *47*(4), 315–351. https://doi.org/10.1139/E09-076

Darbyshire, F. A., Bastow, I., Forte, A., Hobbs, T., Calvel, A., Gonzalez-Monteza, A., & Schow, B. (2015). Variability and origin of seismic anisotropy across eastern Canada: Evidence from shear wave splitting measurements. *Journal of Geophysical Research: Solid Earth*, *120*(12), 8404–8421. https://doi.org/10.1002/2015JB012228

Darbyshire, F. A., Bastow, I., Petrescu, L., Gilligan, A., & Thompson, D. (2017). A tale of two orogens: Crustal processes in the Proterozoic Trans-Hudson and Grenville Orogens, eastern Canada. *Tectonics*, *36*(8), 1633–1659. https://doi.org/10.1002/2017TC004479

Darbyshire, F. A., Dahl-Jensen, T., Larsen, T. B., Voss, P. H., & Joyal, G. (2018). Crust and uppermost-mantle structure of Greenland and the Northwest Atlantic from Rayleigh wave group velocity tomography. *Geophysical Journal International*, *212*(3), 1546–1569. https://doi.org/10.1093/gji/ggx479

Darbyshire, F. A., & Lebedev, S. (2009). Rayleigh wave phase-velocity heterogeneity and multilayered azimuthal anisotropy of the Superior Craton, Ontario. *Geophysical Journal International*, *176*(1), 215–234. https://doi.org/10.1111/j.1365-246X.2008.03982.x

Debayle, E., & Kennett, B. (2000). The Australian continental upper mantle: Structure and deformation inferred from surface waves. *Journal of Geophysical Research: Solid Earth*, *105*(B11), 25423–25450. https://doi.org/10.1029/2000JB900212

Deschamps, F., Lebedev, S., Meier, T., & Trampert, J. (2008). Azimuthal anisotropy of Rayleigh-wave phase velocities in the east-central United States. *Geophysical Journal International*, *173*(3), 827–843. https://doi.org/10.1111/j.1365-246X.2008.03751.x

Eaton, D., Adams, J., Asudeh, I., Atkinson, G., Bostock, M., Cassidy, J., & Unsworth, M. (2005). Investigating Canada's lithosphere and earthquake hazards with portable arrays. *EOS*, *86*, 169–173. https://doi.org/10.1029/eost2005EO17

Ekström, G., Abers, G. A., & Webb, S. C. (2009). Determination of surface-wave phase velocities across USArray from noise and Aki's spectral formulation. *Geophysical Research Letters*, *36*(18). https://doi.org/10.1029/2009GL039131

Foster, A., Darbyshire, F., & Schaeffer, A. (2020). Anisotropic structure of the central north American craton surrounding the mid-continent rift: Evidence from Rayleigh waves. *Precambrian Research*, *342*, 105662. https://doi.org/10.1016/j.precamres.2020.105662

Fountain, D. M., Christensen, N. I., Pakiser, L. C., & Mooney, W. D.(1989). Composition of the continental crust and upper mantle: A review. *Geophysical framework of the continental United States* (Vol. 172, pp. 711–742). Geological Society of America.

Funck, T., Jackson, H. R., Louden, K. E., Dehler, S. A., & Wu, Y. (2004). Crustal structure of the northern Nova Scotia rifted continental margin (eastern Canada). *Journal of Geophysical Research: Solid Earth*, *109*(B9). https://doi.org/10.1029/2004JB003008

Geological Survey of Canada. (1989). Canadian National Seismograph Network. (Dataset). International Federation of Digital Seismograph Networks. https://doi.org/10.7914/SN/CN

Gilligan, A., Bastow, I. D., Watson, E., Darbyshire, F. A., Levin, V., & Menke, W. (2016). Lithospheric deformation in the Canadian appalachians: Evidence from shear wave splitting. *Geophysical Journal International*, *206*(2), 1273–1280. https://doi.org/10.1093/gji/ggw207

Golos, E., Fang, H., Yao, H., Zhang, H., Burdick, S., Vernon, F., & Van der Hilst, R. (2018). Shear wave tomography beneath the United States using a joint inversion of surface and body waves. *Journal of Geophysical Research: Solid Earth*, *123*(6), 5169–5189. https://doi.org/10.1029/2017JB014894

Green, R. G., Priestley, K. F., & White, R. S. (2017). Ambient noise tomography reveals upper crustal structure of Icelandic rifts. *Earth and Planetary Science Letters*, *466*, 20–31. https://doi.org/10.1016/j.epsl.2017.02.039

Guo, Z., Chen, Y. J., Ning, J., Yang, Y., Afonso, J. C., & Tang, Y. (2016). Seismic evidence of on-going sublithosphere upper mantle convection for intra-plate volcanism in Northeast China. *Earth and Planetary Science Letters*, *433*, 31–43. https://doi.org/10.1016/j.epsl.2015.09.035

Hall, J., Marillier, F., & Dehler, S. (1998). Geophysical studies of the structure of the Appalachian orogen in the Atlantic borderlands of Canada. *Canadian Journal of Earth Sciences*, *35*(11), 1205–1221. https://doi.org/10.1139/e98-075

Hammer, P. T., Clowes, R. M., Cook, F. A., van der Velden, A. J., & Vasudevan, K. (2010). The Lithoprobe trans-continental lithospheric cross sections: Imaging the internal structure of the north American continent. *Canadian Journal of Earth Sciences*, *47*(5), 821–857. https://doi.org/10.1139/E10-036

Hibbard, J. P., van Staal, C. R., & Miller, B. V. (2007). Links among Carolinia, Avalonia, and Ganderia in the Appalachian peri-Gondwanan realm. *Geological Society of America Special Papers*, *433*, 291–311. https://doi.org/10.1130/2007.2433(14)

Hibbard, J. P., van Staal, C. R., & Rankin, D. W. (2007). A comparative analysis of pre-Silurian crustal building blocks of the northern and the southern Appalachian orogen. *American Journal of Science*, *307*(1), 23–45. https://doi.org/10.2475/01.2007.02

Hughes, S., & Luetgert, J. H. (1991). Crustal structure of the western New England Appalachians and the Adirondack Mountains. *Journal of Geophysical Research: Solid Earth*, *96*(B10), 16471–16494. https://doi.org/10.1029/91JB01657

Hunter, J. D. (2007). Matplotlib: A 2D graphics environment. *Computing in Science & Engineering*, *9*(3), 90–95. https://doi.org/10.1109/MCSE.2007.55

Hynes, A., & Rivers, T. (2010). Protracted continental collision—Evidence from the Grenville orogen. *Canadian Journal of Earth Sciences*, *47*(5), 591–620. https://doi.org/10.1139/E10-003

IRIS Transportable Array. (2003). USArray transportable array. (Dataset). International Federation of Digital Seismograph Networks. https://doi.org/10.7914/SN/TA

Kamo, S. L., Gower, C. F., & Krogh, T. E. (1989). Birthdate for the Iapetus ocean? A precise U-Pb zircon and baddeleyite age for the long range dikes, southeast Labrador. *Geology*, *17*(7), 602–605. https://doi.org/10.1130/0091-7613(1989)017<0602:BFTLOA>2.3.CO;2

Kamo, S. L., Krogh, T., & Kumarapeli, P. (1995). Age of the Grenville dyke swarm, Ontario-Quebec: Implications for the timing of lapetan rifting. *Canadian Journal of Earth Sciences*, *32*(3), 273–280. https://doi.org/10.1139/e95-022

Kao, H., Behr, Y., Currie, C. A., Hyndman, R., Townend, J., Lin, F.-C., & He, J. (2013). Ambient seismic noise tomography of Canada and adjacent regions: Part I. Crustal structures. *Journal of Geophysical Research: Solid Earth*, *118*(11), 5865–5887. https://doi.org/10.1002/2013JB010535

Kennett, B. L., Engdahl, E., & Buland, R. (1995). Constraints on seismic velocities in the Earth from traveltimes. *Geophysical Journal International*, *122*(1), 108–124. https://doi.org/10.1111/j.1365-246X.1995.tb03540.x

Köhler, A., Weidle, C., & Maupin, V. (2011). Directionality analysis and Rayleigh wave tomography of ambient seismic noise in southern Norway. *Geophysical Journal International*, *184*(1), 287–300. https://doi.org/10.1111/j.1365-246X.2010.04830

Kuponiyi, A. P., Kao, H., van Staal, C. R., Dosso, S. E., Cassidy, J. F., & Spence, G. D. (2017). Upper crustal investigation of the Gulf of Saint Lawrence region, eastern Canada using ambient noise tomography. *Journal of Geophysical Research: Solid Earth*, *122*(7), 5208–5227. https://doi.org/10.1002/2016JB013865

Levin, V., Servali, A., Van Tongeren, J., Menke, W., & Darbyshire, F. A. (2017). *Crust-mantle boundary in Eastern North America, from the (oldest) craton to the (youngest) rift* (Vol. 526, pp. 107–131). Geological Society of America Special Paper. https://doi.org/10.1130/2017.2526(06)

Li, C., Gao, H., & Williams, M. L. (2020). Seismic characteristics of the eastern North American crust with Ps converted waves: Terrane accretion and modification of continental crust. *Journal of Geophysical Research: Solid Earth*, *125*(5), e2019JB018727. https://doi.org/10.1029/2019JB018727

Li, C., Gao, H., Williams, M. L., & Levin, V. (2018). Crustal thickness variation in the northern Appalachian Mountains: Implications for the geometry of 3-D tectonic boundaries within the crust. *Geophysical Research Letters*, *45*(12), 6061–6070. https://doi.org/10.1029/2018GL078777

Lin, F.-C., Moschetti, M. P., & Ritzwoller, M. H. (2008). Surface wave tomography of the western United States from ambient seismic noise: Rayleigh and Love wave phase velocity maps. *Geophysical Journal International*, *173*(1), 281–298. https://doi.org/10.1111/j.1365-246X.2008.03720.x

Long, M. D., Jackson, K. G., & McNamara, J. F. (2016). SKS splitting beneath transportable array stations in eastern North America and the signature of past lithospheric deformation. *Geochemistry, Geophysics, Geosystems*, *17*(1), 2–15. https://doi.org/10.1002/2015GC006088

Ludden, J., & Hynes, A. (2000). The Lithoprobe Abitibi-Grenville transect: Two billion years of crust formation and recycling in the Precambrian shield of Canada. *Canadian Journal of Earth Sciences*, *37*(2–3), 459–476. https://doi.org/10.1139/e99-120

Macdonald, F., Ryan-Davis, J., Coish, R., Crowley, J., & Karabinos, P. (2014). A newly identified Gondwanan terrane in the northern appalachian mountains: Implications for the Taconic orogeny and closure of the Iapetus ocean. *Geology*, *42*(6), 539–542. https://doi.org/10.1130/G35659.1

Martignole, J., & Calvert, A. (1996). Crustal-scale shortening and extension across the Grenville province of western Quebec. *Tectonics*, *15*(2), 376–386. https://doi.org/10.1029/95TC03748

McLellan, M., Schaeffer, A. J., & Audet, P. (2018). Structure and fabric of the crust and uppermost mantle in the northern Canadian Cordillera from Rayleigh-wave tomography. *Tectonophysics*, *724*, 28–41. https://doi.org/10.1016/j.tecto.2018.01.011

Menke, W., Levin, V., & Darbyshire, F. A. (2012). Deep structure of three continental sutures in eastern North America (QM-III). (Dataset). International Federation of Digital Seismograph Networks. https://doi.org/10.7914/SN/X8_2012

Menke, W., Skryzalin, P., Levin, V., Harper, T., Darbyshire, F. A., & Dong, T. (2016). The northern appalachian anomaly: A modern asthenospheric upwelling. *Geophysical Research Letters*, *43*(19), 173–179. https://doi.org/10.1002/2016GL070918

Musacchio, G., Mooney, W. D., Luetgert, J. H., & Christensen, N. I. (1997). Composition of the crust in the Grenville and appalachian provinces of north America inferred from Vp/Vs ratios. *Journal of Geophysical Research: Solid Earth*, *102*(B7), 15225–15241. https://doi.org/10.1029/96JB03737

Pawlak, A., Eaton, D. W., Darbyshire, F., Lebedev, S., & Bastow, I. D. (2012). Crustal anisotropy beneath Hudson Bay from ambient noise tomography: Evidence for post-orogenic lower-crustal flow? *Journal of Geophysical Research: Solid Earth*, *117*(B8). https://doi.org/10.1029/2011JB009066

Petrescu, L., Bastow, I., Darbyshire, F. A., Gilligan, A., Bodin, T., Menke, W., & Levin, V. (2016). Three billion years of crustal evolution in eastern Canada: Constraints from receiver functions. *Journal of Geophysical Research: Solid Earth*, *121*(2), 788–811. https://doi.org/10.1002/2015JB012348

Petrescu, L., Darbyshire, F. A., Bastow, I., Totten, E., & Gilligan, A. (2017). Seismic anisotropy of Precambrian lithosphere: Insights from Rayleigh wave tomography of the eastern Superior Craton. *Journal of Geophysical Research: Solid Earth*, *122*(5), 3754–3775. https://doi.org/10.1002/2016JB013599

Prieto, G., Lawrence, J., & Beroza, G. (2009). Anelastic Earth structure from the coherency of the ambient seismic field. *Journal of Geophysical Research: Solid Earth*, *114*(B7). https://doi.org/10.1029/2008JB006067

Ritsema, J., & Lekić, V. (2020). Heterogeneity of seismic wave velocity in Earth's mantle. *Annual Review of Earth and Planetary Sciences*, *48*, 377–401. https://doi.org/10.1146/annurev-earth-082119-065909

Rivers, T. (1997). Lithotectonic elements of the Grenville province: Review and tectonic implications. *Precambrian Research*, *86*(3–4), 117–154. https://doi.org/10.1016/S0301-9268(97)00038-7

Rivers, T. (2008). Assembly and preservation of lower, mid, and upper orogenic crust in the Grenville Province—Implications for the evolution of large hot long-duration orogens. *Precambrian Research*, *167*(3–4), 237–259. https://doi.org/10.1016/j.precamres.2008.08.005

Rivers, T. (2015). Tectonic setting and evolution of the Grenville orogen: An assessment of progress over the last 40 years. *Geoscience Canada*, *42*(1). https://doi.org/10.12789/geocanj.2014.41.057

Rivers, T., Ketchum, J., Indares, A., & Hynes, A. (2002). The high pressure belt in the Grenville Province: Architecture, timing, and exhumation. *Canadian Journal of Earth Sciences*, *39*(5), 867–893. https://doi.org/10.1139/e02-025

Rivers, T., Martignole, J., Gower, C., & Davidson, A. (1989). New tectonic divisions of the Grenville Province, southeast Canadian shield. *Tectonics*, *8*(1), 63–84. https://doi.org/10.1029/TC008i001p00063

Sadeghisorkhani, H., Gudmundsson, Ó., & Tryggvason, A. (2018). GSpecDisp: A Matlab GUI package for phase-velocity dispersion measurements from ambient-noise correlations. *Computers & Geosciences*, *110*, 41–53. https://doi.org/10.1016/j.cageo.2017.09.006

Schaeffer, A., & Lebedev, S. (2013). Global shear speed structure of the upper mantle and transition zone. *Geophysical Journal International*, *194*(1), 417–449. https://doi.org/10.1093/gji/ggt095

Schaeffer, A., & Lebedev, S. (2014). Imaging the North American continent using waveform inversion of global and USArray data. *Earth and Planetary Science Letters*, *402*, 26–41. https://doi.org/10.1016/j.epsl.2014.05.014

SEIS-UK (2013). *QM-III Network – Atlantic Canada* [Data set]. International Federation of Digital Seismograph Networks. https://www.fdsn.org/networks/detail/Y6_2013/

Shapiro, N. M., & Campillo, M. (2004). Emergence of broadband Rayleigh waves from correlations of the ambient seismic noise. *Geophysical Research Letters*, *31*(7). https://doi.org/10.1029/2004GL019491

Shapiro, N. M., Campillo, M., Stehly, L., & Ritzwoller, M. H. (2005). High-resolution surface-wave tomography from ambient seismic noise. *Science*, *307*(5715), 1615–1618. https://doi.org/10.1126/science.1108339

Shen, W., & Ritzwoller, M. H. (2016). Crustal and uppermost mantle structure beneath the United States. *Journal of Geophysical Research: Solid Earth*, *121*(6), 4306–4342. https://doi.org/10.1002/2016JB012887

Smith, M. L., & Dahlen, F. (1973). The azimuthal dependence of Love and Rayleigh wave propagation in a slightly anisotropic medium. *Journal of Geophysical Research*, *78*(17), 3321–3333. https://doi.org/10.1029/JB078i017p03321

Stockmal, G., Colman-Sadd, S., Keen, C., O'Brien, S., & Quinlan, G. (1987). Collision along an irregular margin: A regional plate tectonic interpretation of the Canadian appalachians. *Canadian Journal of Earth Sciences*, *24*(6), 1098–1107. https://doi.org/10.1139/e87-107

Tarantola, A. (2005). *Inverse problem theory and methods for model parameter estimation*. SIAM. https://doi.org/10.1137/1.9780898717921

Tian, Y., & Ritzwoller, M. H. (2015). Directionality of ambient noise on the Juan de Fuca plate: Implications for source locations of the primary and secondary microseisms. *Geophysical Journal International*, *201*(1), 429–443. https://doi.org/10.1093/gji/ggv024

van der Lee, S., & Frederiksen, A. (2005). Surface wave tomography applied to the North American upper mantle. *Seismic Earth: Array Analysis of Broadband Seismograms*, *157*, 67–80. https://doi.org/10.1029/157GM05

van Staal, C. R., & Barr, S. (2012). Lithospheric architecture and tectonic evolution of the Canadian Appalachians and associated Atlantic margin. *Geological Association of Canada Special Paper*, *49*, 41–95.

van Staal, C. R., Barr, S. M., & Murphy, J. B. (2012). Provenance and tectonic evolution of Ganderia: Constraints on the evolution of the Iapetus and Rheic oceans. *Geology*, *40*(11), 987–990. https://doi.org/10.1130/G33302.1

van Staal, C. R., Barr, S. M., Waldron, J. W., Schofield, D. I., Zagorevski, A., & White, C. E. (2021). Provenance and Paleozoic tectonic evolution of Ganderia and its relationships with Avalonia and Megumia in the Appalachian-Caledonide orogen. *Gondwana Research*, *98*, 212–243. https://doi.org/10.1016/j.gr.2021.05.025

van Staal, C. R., Whalen, J. B., Valverde-Vaquero, P., Zagorevski, A., & Rogers, N. (2009). Pre-Carboniferous, episodic accretion-related, orogenesis along the Laurentian margin of the northern Appalachians. *Geological Society, London, Special Publications*, *327*(1), 271–316. https://doi.org/10.1144/SP327.13

van Staal, C. R., & Zagorevski, A. (2020). Accretion, soft and hard collision: Similarities, differences and an Application from the Newfoundland Appalachian orogen. *Geoscience Canada*, *47*(3), 103–118. https://doi.org/10.12789/geocanj.2020.47.161

Villemaire, M., Darbyshire, F. A., & Bastow, I. (2012). P-wave tomography of eastern North America: Evidence for mantle evolution from Archean to Phanerozoic, and modification during subsequent hot spot tectonism. *Journal of Geophysical Research: Solid Earth*, *117*(B12). https://doi.org/10.1029/2012JB009639

Wessel, P., Smith, W. H., Scharroo, R., Luis, J., & Wobbe, F. (2013). Generic mapping tools: Improved version released. *EOS*, *94*(45), 409–410. https://doi.org/10.1002/2013EO450001

Whitmeyer, S. J., & Karlstrom, K. E. (2007). Tectonic model for the Proterozoic growth of north America. *Geosphere*, *3*(4), 220–259. https://doi.org/10.1130/GES00055.1

Williams, H., Colman-Sadd, S., & Swinden, H. (1988). *Tectonic-stratigraphic Subdivisions of Central Newfoundland. Current Research, Part B* (Vol. 88, pp. 91–98). Geological Survey of Canada, Paper. https://doi.org/10.4095/122414

Wilson, R. A., van Staal, C. R., & Kamo, S. L. (2017). Rapid transition from the Salinic to Acadian orogenic cycles in the northern appalachian orogen: Evidence from northern New Brunswick, Canada. *American Journal of Science*, *317*(4), 449–482. https://doi.org/10.2475/04.2017.02

Withjack, M. O., Olsen, P. E., & Schlische, R. W. (1995). Tectonic evolution of the Fundy rift basin, Canada: Evidence of extension and shortening during passive margin development. *Tectonics*, *14*(2), 390–405. https://doi.org/10.1029/94TC03087

Withjack, M. O., Schlische, R. W., & Baum, M. S. (2009). Extensional development of the Fundy rift basin, southeastern Canada. *Geological Journal*, *44*(6), 631–651. https://doi.org/10.1002/gj.1186

Yang, B. B., Liu, Y., Dahm, H., Liu, K. H., & Gao, S. S. (2017). Seismic azimuthal anisotropy beneath the eastern United States and its geodynamic implications. *Geophysical Research Letters*, *44*(6), 2670–2678. https://doi.org/10.1002/2016GL071227

Yang, Y., Li, A., & Ritzwoller, M. H. (2008). Crustal and uppermost mantle structure in southern Africa revealed from ambient noise and teleseismic tomography. *Geophysical Journal International*, *174*(1), 235–248. https://doi.org/10.1111/j.1365-246X.2008.03779.x

Yang, Y., Ritzwoller, M. H., Levshin, A. L., & Shapiro, N. M. (2007). Ambient noise Rayleigh wave tomography across Europe. *Geophysical Journal International*, *168*(1), 259–274. https://doi.org/10.1111/j.1365-246X.2006.03203.x

Yao, H., van Der Hilst, R. D., & De Hoop, M. V. (2006). Surface-wave array tomography in SE Tibet from ambient seismic noise and two-station analysis—I. Phase velocity maps. *Geophysical Journal International*, *166*(2), 732–744. https://doi.org/10.1111/j.1365-246X.2006.03028.x

Yuan, H., French, S., Cupillard, P., & Romanowicz, B. (2014). Lithospheric expression of geological units in central and eastern North America from full waveform tomography. *Earth and Planetary Science Letters*, *402*, 176–186. https://doi.org/10.1016/j.epsl.2013.11.057